Check for updates

Angewandte Chemie International Edition

Angewandte International Edition Chemie

How to cite: *Angew. Chem. Int. Ed.* **2026**, e7908002
doi.org/10.1002/anie.7908002

RESEARCH ARTICLE

Reusable and Robust Hydrogel With Dynamic Sacrificial S—S Bonds: In Situ Construction of an Integrated SEI/Hydrogel Interface for Highly Stable Zn–I_2 Batteries

Peng Li[1] | Jinping Wu[1] | Zihan Zhu[1] | Jing Tang[1] | Ling Zhu[1] | Liya Wang[1] | Xuan Tang[1] | Fangfang Ruan[1] | Huibing He[1] | Ning Zhao[2] | Dongdong Li[1]

[1]Guangxi Key Laboratory of Electrochemical Energy Materials, Guangxi Colleges and Universities Key Laboratory of Applied Chemistry Technology and Resource Development, School of Chemistry and Chemical Engineering, Guangxi University, Nanning, China | [2]Beijing National Laboratory For Molecular Sciences (BNLMS), Laboratory of Polymer Physics and Chemistry, Institute of Chemistry, Chinese Academy of Sciences, University of Chinese Academy of Sciences, Beijing, China

Correspondence: Ning Zhao (zhaoning@iccas.ac.cn) | Dongdong Li (lidd@gxu.edu.cn)

Received: 15 August 2026 | **Revised:** 25 September 2026 | **Accepted:** 17 October 2026

Keywords: aqueous zinc–iodine battery | hydrogel | interfacial regulation | reusable

ABSTRACT

The trade-off among mechanical strength, ionic conductivity, and interfacial stability remains a core challenge for high-performance hydrogel interfacial layers. Herein, an integrated SEI/polyurea–polyurethane hydrogel (PUMA) interface was constructed on the Zn anode via in situ gelation coupled with interfacial electrochemical reduction. Polyurea–polyurethane hard segments containing octuple H-bonds, Zn^{2+} coordination bonds, and dynamic S—S bonds reinforce PUMA through multi-level energy dissipation and suppress side reactions by regulating interfacial water. Polyanionic soft segments rich in carboxyl and sulfonic acid groups construct low-barrier, ion-selective pathways, optimizing Zn^{2+} transport and deposition by solvation regulation and mitigation of concentration polarization. Crucially, interfacial sacrificial S—S bonds undergo cleavage during electrochemical reduction, generating an integrated SEI/PUMA interface with enhanced interfacial stability. The dynamic polyanionic network also blocks polyiodide shuttling and enables thermal reprocessing. Consequently, PUMA@Zn achieves a Zn^{2+} transference number of 0.79 and symmetric cell cycling for 5080 h (1 mA cm^{-2} and 0.5 mAh cm^{-2}). PUMA@Zn//I_2 cells retain 88% capacity after 43 000 cycles at 4 A g^{-1} and operate for over 11 000 cycles even at high iodine loading (16.58 mg cm^{-2}). This strategy provides a novel pathway to achieve robust, ion-conductivity, and chemically bonded hydrogel–metal interfaces for high-performance aqueous batteries.

1 | Introduction

The growing global demand for clean energy and advanced energy storage calls for safe, low-cost, high-performance rechargeable batteries [1, 2]. Aqueous zinc–iodine (Zn–I_2) batteries possess outstanding advantages, including high theoretical specific capacity, intrinsic safety, abundant zinc and iodine resources, and low cost, showing broad application prospects in emerging energy storage [3–6]. However, their practical application faces dual challenges: On the Zn anode side, severe hydrogen evolution reaction (HER), corrosion, and passivation cause interfacial polarization and anode failure [7, 8], while nonuniform Zn deposition promotes dendrite growth and poses safety risks [9, 10]. On the iodine cathode side, highly water-soluble polyiodide anions (e.g., I_3^- and I_5^-) undergo a "shuttle effect" [11–13], disrupting the solid electrolyte interphase

All rights reserved, including rights for text and data mining and training of artificial intelligence technologies or similar technologies.
© 2026 Wiley-VCH GmbH

(SEI) and further aggravating Zn anode side reactions, ultimately forming a vicious cycle of "iodine shuttling–anode corrosion–exacerbated dendrite growth", which severely compromises battery stability [14]. Currently, Zn–I_2 battery stability has improved via cathode host and catalytic material design [15, 16], electrolyte engineering [17, 18], separator modification [19, 20], and construction of artificial interfacial protective layers [21, 22]. Since interfacial chemistry and microstructure critically govern electrochemical reversibility, artificial interfacial protective layers have attracted substantial research interest [23, 24]. Among them, hydrogel interfacial protective layers, with their precisely tunable functional groups and 3D crosslinked networks, exhibit great potential for stabilizing electrode interfaces [25–27].

However, hydrogels require both high mechanical strength and high ionic conductivity, properties that are inherently conflicting, posing a major challenge in developing high-performance hydrogel interfacial layers [28, 29]. This is because ionic conductivity is strongly dependent on hydrogel water content and chain mobility: dense crosslinking enhances mechanical strength but restricts chain motion and reduces swelling, thereby hindering Zn^{2+} transport; conversely, reducing crosslink density facilitates ion conduction but weakens mechanical strength; meanwhile, excessive swelling increases free-water content and aggravates interfacial side reactions [30]. To overcome the above trade-off, current approaches mainly include composite reinforcement and Hofmeister effect regulation. The former enhances gel strength by incorporating inorganic fillers; however, significant mismatches in modulus and polarity between fillers and polymer matrix lead to poor interfacial compatibility; simultaneously, excessive filler loading inevitably restricts chain motion and thus hinders ionic transport [28, 31, 32]. The Hofmeister effect utilizes specific ions to modulate the dielectric constant and H-bonding networks, thereby altering molecular-chain aggregation states and concurrently enhancing both mechanical strength and ionic conductivity. Nevertheless, high-strength gel fabrication exhibits ion specificity (e.g., SO_4^{2-}), limiting compatibility with diverse zinc-salt electrolytes [33–36]. Moreover, conventional hydrogels generally exhibit a low Zn^{2+} transference number, leading to concentration polarization, nonuniform interfacial electric fields, and dendrite growth [37, 38].

Efficiently constructing a Zn anode/hydrogel interface with both long-term conformal contact and high chemical stability is another critical, unmet challenge [39]. During cycling, the intrinsic solid–solid interface between the Zn anode and hydrogel readily develops interfacial gaps under repeated deformation, disrupting ion transport, raising interfacial resistance, and causing localized Zn deposition in the limited-contact regions [40, 41]. Conventional approaches of directly covering the electrode with a preformed hydrogel further aggravate interfacial discontinuities and accelerate interfacial failure [21]. In contrast, in situ gelation can form a gap-free, tightly conformal interface, ensuring uniform interfacial mass transfer and offering a simple one-step fabrication process. However, as the Zn anode undergoes continuous dynamic changes during charge/discharge cycling, the gel layer struggles to maintain long-term tight adhesion and interfacial structural integrity [42, 43]. Moreover, the generally poor interfacial compatibility between polymers and Zn often leads to spontaneous detachment upon hydrogel full swelling, severely undermining interfacial stability. Although significant advances have been achieved in enhancing interfacial bonding by introducing adhesive functional groups such as catechol [44] and amide [45], the high water content of the hydrogel continuously induces interfacial side reactions, leading to progressive interfacial degradation over cycling.

To address the aforementioned challenges, we herein innovatively constructed an integrated SEI/polyurea–polyurethane hydrogel (PUMA) interfacial protective layer on the Zn anode via in situ gelation and in situ electrochemical reduction, simultaneously achieving high mechanical strength, a high Zn^{2+} transference number, and excellent interfacial stability (Figure 1). The hydrogel consists of a microphase-separated, dynamically crosslinked network. The polyurea–polyurethane hard segments contain octuple H-bonds, Zn^{2+} coordination bonds, and dynamic S—S bonds. This multi-bond architecture forms a rigid framework that imparts ultra-high mechanical strength to PUMA via multi-level energy dissipation, strengthens interfacial anchoring through synergistic bonding, and suppresses interfacial side reactions by H-bond-mediated water confinement, thereby significantly enhancing the cohesive strength and interfacial stability of the hydrogel. The polyanionic soft segments, rich in carboxyl and sulfonic acid groups, ensure fast, uniform Zn^{2+} transport via chain-coordination hopping transport, remove interfacial water through competitive adsorption, and accelerate Zn^{2+} deposition by lowering the desolvation energy barrier, thereby guiding efficient and dendrite-free Zn deposition. More critically, interfacial sacrificial S—S bonds can partially cleave during electrochemical reduction, driving in situ formation of an integrated organic–inorganic hybrid SEI/PUMA interface. Combined with the interfacial synergistic bonding arising from octuple H-bonds, Zn^{2+} coordination bonds, and electron-rich S—S bonds, this integrated SEI/PUMA interface ensures robust adhesion and long-term conformal contact between PUMA and the Zn anode.

This integrated SEI/PUMA interface not only reconciles high mechanical strength, efficient ion conduction, and excellent interfacial stability, but also effectively regulates the interfacial environment. Its polyanionic network constructs a high-density electrostatic shielding field that repels polyiodide anions and SO_4^{2-}, and raises the Zn^{2+} transference number, thereby suppressing the shuttle effect and concentration polarization to enable highly stable Zn–I_2 batteries. Through multiscale regulation, PUMA achieves a fracture strain of 640% and a fracture strength as high as 2.68 MPa, far exceeding conventional hydrogels. The PUMA@Zn anode achieves a high Zn^{2+} transference number of 0.79. The symmetric cell operates stably for over 5080 h at 1 mA cm^{-2} and 0.5 mAh cm^{-2}, and maintains stability for over 1000 h even under harsh intermittent conditions (10 mA cm^{-2} and 5 mAh cm^{-2} with 30 h open-circuit resting periods). The Zn–I_2 full cell retains 88% of its initial capacity after 43 000 cycles at 4 A g^{-1}. Moreover, the dynamically crosslinked network, comprising abundant H-bonds and S—S bonds, enables shape reconfiguration and cyclic reuse of the gel matrix via hot pressing at 140°C, highlighting its distinct sustainability advantage over conventional covalently crosslinked hydrogels. This integrated interfacial molecular engineering strategy offers valuable insights for the development of highly stable aqueous batteries.

15213773, 0, Downloaded from https://onlinelibrary.wiley.com/doi/10.1002/anie.7908002 by Li Dongdong - Guangxi University , Wiley Online Library on [24/10/2026]. See the Terms and Conditions (https://onlinelibrary.wiley.com/terms-and-conditions) on Wiley Online Library for rules of use; OA articles are governed by the applicable Creative Commons License

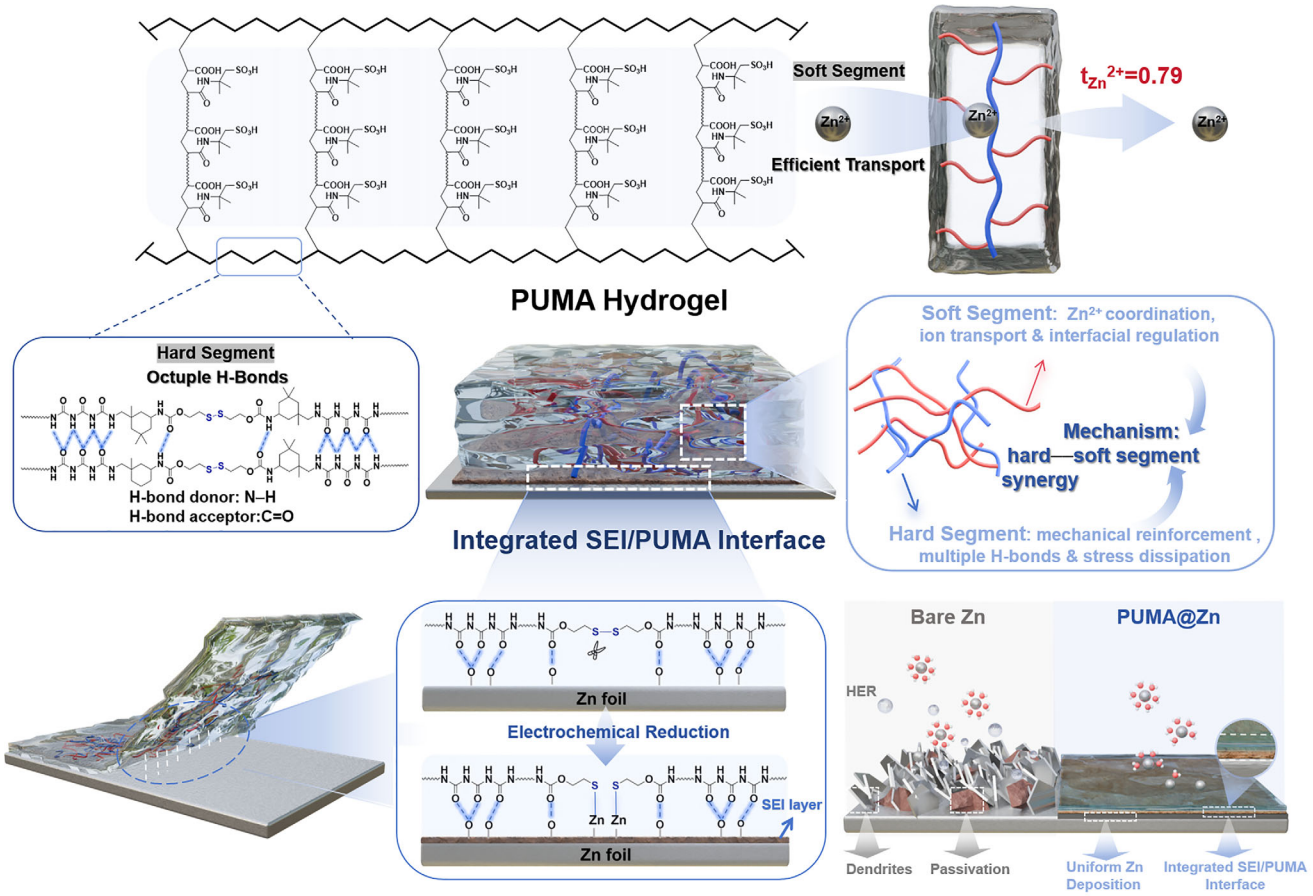


FIGURE 1 | Schematic illustration of the structure and functions of the integrated SEI/polyurea–polyurethane hydrogel interfacial protective layer.

2 | Results and Discussion

2.1 | Structural Design and Interfacial Properties of PUMA

As shown in Figure S1, a polyurea hard segment was synthesized from isophorone diisocyanate (IPDI) and urea, followed by incorporation of dynamic S—S bond units using bis(2-hydroxyethyl) disulfide (HEDS) and end-capping with hydroxyethyl methacrylate (HEMA) to introduce terminal vinyl groups, ultimately yielding the multifunctional macromolecular crosslinker PU–SS–HEMA. Subsequently, PU–SS–HEMA was copolymerized in situ with acrylic acid (AA) and 2-acrylamido-2-methylpropanesulfonic acid (AMPS) on the Zn anode surface to construct the PUMA protective layer. The polymer chain architecture integrates polyurea–polyurethane hard segments, dynamic disulfide units, and AA/AMPS-derived polyanionic soft segments, providing a molecular structural foundation for simultaneously achieving high mechanical strength, efficient Zn^{2+} transport, and interfacial chemical regulation.

Fourier transform infrared spectroscopy (FTIR) and x-ray photoelectron spectroscopy (XPS) confirmed the successful fabrication of PUMA. As shown in Figure 2a, the characteristic —N=C=O peak at 2260 cm^{-1} observed in IPDI disappeared entirely in PU–SS–HEMA, indicating complete reaction of isocyanate groups [46]. Concurrently, a broad N—H stretching vibration appeared near 3300 cm^{-1}, and distinct C=O peaks attributable to urethane/urea bonds emerged within the 1650–1700 cm^{-1} region [47, 48], collectively confirming the successful construction of the polyurea–polyurethane hard-segment backbone. Moreover, in PU–SS–HEMA, a distinct C=C peak at 1630 cm^{-1} confirms the successful incorporation of vinyl groups at chain ends, thereby providing reactive sites for subsequent in situ crosslinking. After in situ thermally initiated polymerization, the PUMA retains the N—H and O—H/C=O absorption bands, which display significant broadening and distinct blue shifts (Figure 2b), indicating the formation of extensive H-bonding networks among the polar N—H, O—H, and C=O functional groups [49]. This multiple H-bonding network constitutes a key molecular architecture underpinning the exceptional mechanical properties and structural stability of the PUMA. The XPS spectra of PUMA@Zn show that the C 1s and O 1s signals are markedly intensified compared with those of Bare Zn, accompanied by the appearance of N 1s and S 2p peaks (Figure S2a), confirming the successful incorporation of N- and S-containing functional groups into PUMA. In high-resolution XPS analysis, the S 2p signal at about 169.0 eV corresponds to the sulfonic acid groups in AMPS, while the characteristic doublet near 163.0 eV is attributed to S—S bonds (Figure 2c) [50, 51]; the N 1s peak at 399.8 eV reflects the —NH—CO— linkage in polyurea–polyurethane hard segments (Figure 2d) [52]; and the C 1s spectrum shows the coexistence of C—C/C—H, C—O/C—N/C—S, N—C=O, and O—C=O multiple chemical states (Figure S2b), collectively confirming successful PUMA network formation. In addition, cross-sectional focused ion beam–scanning electron microscopy (FIB–SEM) imaging coupled with energy-dispersive

15213773, 0, Downloaded from https://onlinelibrary.wiley.com/doi/10.1002/anie.7908002 by Li Dongdong - Guangxi University , Wiley Online Library on [24/10/2026]. See the Terms and Conditions (https://onlinelibrary.wiley.com/terms-and-conditions) on Wiley Online Library for rules of use; OA articles are governed by the applicable Creative Commons License

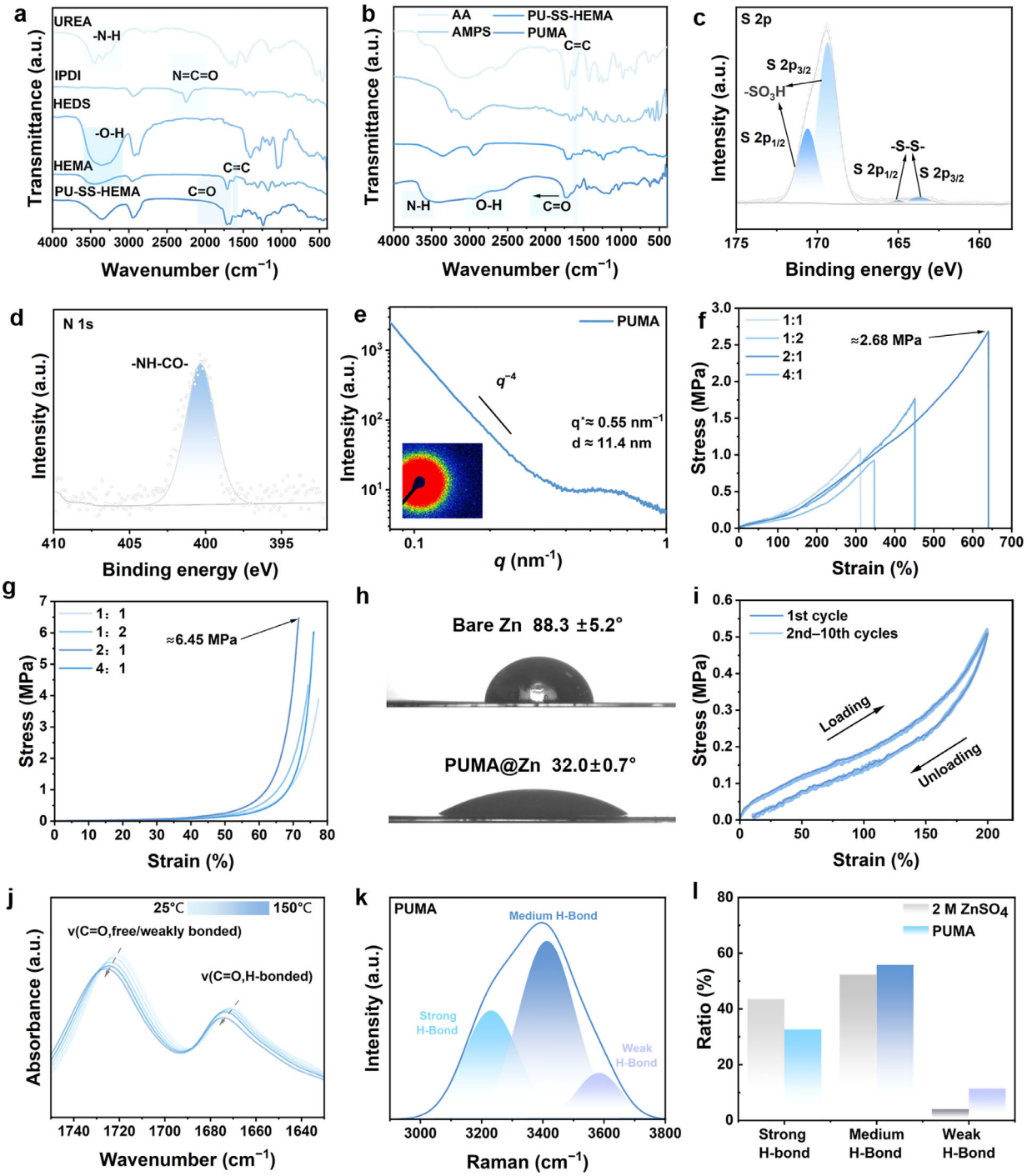


FIGURE 2 | (a) FTIR spectra of UREA, IPDI, HEDS, HEMA, and the PU–SS–HEMA crosslinker. (b) FTIR spectra of AA, AMPS, PU–SS–HEMA, and PUMA. (c, d) High-resolution XPS spectra of S 2p and N 1s for PUMA@Zn. (e) SAXS curve of PUMA (inset: corresponding 2D scattering pattern). (f) Tensile stress–strain curves and (g) compressive stress–strain curves of PUMA prepared with different AA/AMPS mass ratios. (h) Electrolyte contact angles on Bare Zn and PUMA@Zn. (i) Cyclic tensile–recovery stress–strain curves of PUMA (10 cycles). (j) Variable-temperature FTIR spectra of the C═O stretching vibration region in PUMA. (k) Raman peak-fitting curves of the O—H stretching band of water in PUMA. (l) Quantitative comparison of strongly, moderately, and weakly H-bonded water in 2 M $ZnSO_4$ electrolyte and PUMA.

x-ray spectroscopy (EDS) elemental mapping reveals a continuous, dense interface between the PUMA and Zn substrate, with uniform gel thickness (~7.8 μm) and exclusive C, O, S, and N signal localization within the PUMA layer (Figure S3), confirming the successful in situ construction of the PUMA layer on the Zn anode surface.

On the basis of the clarified molecular structure and chemical composition, small-angle x-ray scattering (SAXS) and atomic force microscopy (AFM) further analyzed the nanoscale aggregated structures of the soft and hard segments in PUMA. As shown in Figure 2e, PUMA exhibits a Porod scattering behavior ($\sim q^{-4}$) in the low-q region, accompanied by a distinct scattering

15213773, 0, Downloaded from https://onlinelibrary.wiley.com/doi/10.1002/anie.7908002 by Li Dongdong - Guangxi University , Wiley Online Library on [24/10/2026]. See the Terms and Conditions (https://onlinelibrary.wiley.com/terms-and-conditions) on Wiley Online Library for rules of use; OA articles are governed by the applicable Creative Commons License

signal at q* ≈ 0.55 nm^{-1}, corresponding to a structural scale of approximately 11.4 nm, which provides direct evidence for short-range ordered nanoscale microphase separation in PUMA [49, 53]. The AFM phase image clearly shows uniformly distributed bright and dark domains, with an average size matching the SAXS-obtained characteristic length scale, further confirming distinct microphase separation between hard and soft segments. In this structure, hard segments serve as physical crosslinks to provide high strength, while soft segments impart chain mobility to ensure toughness, collectively enhancing the PUMA's mechanical properties and structural stability. The AFM height image reveals a continuous, intact gel surface with only nanoscale surface fluctuations (Figure S4), indicating the excellent integrity and surface flatness of the PUMA layer. In addition, scanning electron microscopy (SEM) images of the freeze-dried PUMA further reveal a highly interconnected, three-dimensional porous framework within the gel (Figure S5). This structure simultaneously promotes electrolyte infiltration, dissipates localized stress, and establishes continuous Zn^{2+} transport pathways [54]. Collectively, these results demonstrate that the PUMA possesses both an ordered hard–soft segment microphase-separated structure and an interconnected porous framework, providing an important structural foundation for achieving both high mechanical strength and rapid ion transport.

To achieve an optimal balance between mechanical strength and ion transport, the PU–SS–HEMA macromolecular crosslinker content and the AA/AMPS monomer ratio were regulated. Ionic conductivity and Zn//Zn symmetric cell tests (Figures S6, S8, and S11) demonstrate that both crosslinking density and monomer ratio have a pronounced influence on balancing network stability and ion transport efficiency. At a 5 wt% macromolecular crosslinker (PU–SS–HEMA) content and an AA/AMPS mass ratio of 2:1, the PUMA achieves optimal overall performance: ionic conductivity reaches as high as 31.8 mS cm^{-1}, fracture strength reaches 2.68 MPa, and fracture strain attains 640% (Figures 2f and S9); meanwhile, the compressive strength reaches 6.45 MPa at 70% strain (Figure 2g). Compared with representative hydrogel electrolytes or protective layers reported in recent years, PUMA exhibits superior tensile strength while maintaining a high fracture strain, demonstrating an exceptional strength–ductility synergy (Figure S10 and Table S1). Meanwhile, the symmetric cell employing this hydrogel protective layer also shows the best cycling stability, operating stably for over 1300 h at 5 mA cm^{-2} and 2.5 mAh cm^{-2} (Figure S11). The electrolyte contact angle decreases from 88.3 ± 5.2° on Bare Zn to 32.0 ± 0.7° on PUMA@Zn (Figure 2h), indicating markedly improved electrolyte wettability. After repeated folding and severe crumpling, the PUMA layer remains intact and firmly adhered to the Zn foil surface (Figure S12). This arises from the ultrahigh bulk cohesive strength of the PUMA layer endowed by its microphase-separated structure (as shown in Figure S13, a PUMA strip weighing only 0.11 g can stably suspend a 500 g weight), combined with strong interfacial adhesion enabled by abundant polar carboxyl/sulfonic acid groups, dense H-bond network, and zincophilic S—S bonds. The synergistic interaction of these features significantly enhances the stability of the PUMA layer.

The structural stability of the gel layer is crucial for accommodating the continuous Zn anode volume changes and maintaining a stable gel–Zn interface. Cyclic tensile–recovery tests further evaluate the structural durability of PUMA under cyclic mechanical loading. As shown in Figure 2i, the stress–strain curves obtained over 10 consecutive cycles exhibit strong overlap and pronounced hysteresis, indicating that the multiple H-bonds within PUMA enable reversible dissociation and reformation during mechanical deformation, thus achieving multi-level reversible energy dissipation [55, 56]. To further elucidate the molecular origin of this dissipation mechanism, variable-temperature FTIR combined with two-dimensional correlation spectroscopy (2D-COS) was employed to characterize the C═O stretching vibration region. The results show that, upon increasing the temperature from 25 to 150°C, both free (or weakly H-bonded) C═O and H-bonded C═O components shift toward higher wavenumbers, accompanied by narrowed peak widths and gradually decreased intensities, indicating thermally induced weakening and rearrangement of the carbonyl-related hydrogen-bond microenvironments (Figure 2j). The characteristic peaks in the synchronous and asynchronous 2D-COS spectra further reveal that different carbonyl microenvironments exhibit cooperative yet asynchronous responses to thermal perturbation (Figure S14) [57], directly demonstrating that the multiple H-bonds in PUMA function as reversible sacrificial bonds, capable of dissipating stress and thereby enhancing PUMA's bulk cohesion and structural stability. In addition, the dynamically crosslinked network, composed of multiple H-bonds and reversible S—S bonds, enables PUMA fragments to be hot-pressed into a continuous, dense film at 140°C, 5 MPa, demonstrating excellent thermoplasticity and potential for cyclic reuse (Figure S15).

To verify the design advantages of PUMA's molecular architecture, N,N′-methylenebisacrylamide was used to replace the PU–SS–HEMA macromolecular crosslinker to prepare a control hydrogel P(AA-co-AMPS)-MBA without polyurea–polyurethane hard segments and dynamic S—S units. Zn//Zn symmetric cell tests reveal that, at 5 mA cm^{-2} and 2.5 mAh cm^{-2}, P(AA-co-AMPS)-MBA@Zn with the optimal crosslinking degree cycles for only 350 h (Figure S16), far shorter than the 1300 h achieved by PUMA@Zn (Figure S17a). Mechanical testing further confirms that PUMA exhibits significantly enhanced strength, extensibility, and compressive resistance relative to P(AA-co-AMPS)-MBA (Figure S17b,c). The synergistic interplay among microphase separation of hard/soft segments, multiple H-bonding networks, and dynamic S—S units constitutes the core molecular structural basis underpinning PUMA's high mechanical stability. In addition to the advantages of molecular networks and aggregated structures, the densely distributed polar sites in PUMA, including —COOH, —SO_3H, —NHCO—, and N—H/C═O, can also regulate the H-bonding states of water both in the PUMA bulk phase and at the Zn anode interface. Raman deconvolution (Figures 2k and S18) resolves the O—H stretching vibration region of water into three characteristic components: strongly H-bonded water (3229 cm^{-1}), moderately H-bonded water (3412 cm^{-1}), and weakly H-bonded water (3582 cm^{-1}). Quantitative analysis shows that the proportion of strongly H-bonded water decreases from 43% in 2 M $ZnSO_4$ electrolyte to 32% in PUMA, whereas the moderately and weakly H-bonded components rise to become dominant. The decreased contribution of weakly hydrogen-bonded water suggests a reduced population of relatively free water molecules within the PUMA network [22].

15213773, 0, Downloaded from https://onlinelibrary.wiley.com/doi/10.1002/anie.7908002 by Li Dongdong - Guangxi University , Wiley Online Library on [24/10/2026]. See the Terms and Conditions (https://onlinelibrary.wiley.com/terms-and-conditions) on Wiley Online Library for rules of use; OA articles are governed by the applicable Creative Commons License

2.2 | PUMA-Mediated Regulation of Zn^{2+} Transport and Interfacial Properties

Molecular models were constructed using a polyurea–polyurethane hard segment, a carboxyl/sulfonic acid-functionalized flexible soft segment, a dynamic S—S segment, and a primary repeating unit of PUMA. Density functional theory (DFT) calculations were performed to reveal the regulatory mechanism of PUMA on Zn^{2+} transport kinetics and the interfacial microenvironment.

First, the regulatory effects of each structural component on the Zn^{2+} solvation sheath and the interfacial environment at the Zn anode were systematically analyzed. Figure 3a shows the electrostatic potential (ESP) distribution of $[Zn(H2O)_6]^{2+}$, which exhibits a highly localized positive ESP (red region), reflecting extremely strong Zn^{2+}–H_2O coordination, a high desolvation energy barrier, sluggish reaction kinetics, and a propensity for inhomogeneous Zn deposition. Upon PUMA addition, the polar soft segments strongly coordinate with Zn^{2+} through carboxyl and sulfonic acid groups, effectively dispersing the charge density and lowering the positive ESP associated with the solvation sheath. In contrast, the polyurea–polyurethane hard segments exhibit a relatively moderate ESP distribution, resulting in weaker Zn^{2+} binding and a limited influence on Zn^{2+} migration. Migration energy barriers further quantify this difference: the Zn^{2+} migration barrier in the soft-segment model is only 0.59 eV (Figures 3b and S19), markedly lower than that of the hard segment (0.82 eV), directly confirming that the polar soft segments are more favorable for Zn^{2+} migration. Combined with the ESP analysis, these results indicate that the soft segments promote $[Zn(H2O)_6]^{2+}$ desolvation through charge dispersion and polar coordination, thereby accelerating Zn^{2+} transport kinetics, whereas the hard segments bind Zn^{2+} moderately and play a negligible role in Zn^{2+} transport. These results are consistent with the molecular structural characteristics of PUMA, whose microphase-separated hard–soft segment architecture exhibits a clear functional division: the polyurea–polyurethane hard segments form a robust network skeleton that enhances PUMA's cohesive strength and structural stability, whereas the polar soft segments dominate Zn^{2+} coordination, migration, and solvation-shell regulation. These complementary functions synergistically improve both the mechanical strength and Zn^{2+} transport capability of PUMA.

Subsequently, molecular-level analysis revealed how functional groups in PUMA's soft and hard segments interact with Zn^{2+}. As shown in Figure 3c,d, the binding energies of the sulfonic acid and carboxyl groups in the soft segments with Zn^{2+} are −1.08 and −1.03 eV, respectively, more negative than H_2O–Zn^{2+} binding energy (−0.24 eV). This strong preferential binding enables competitive displacement of solvated water from the Zn^{2+} solvation shell, thereby accelerating Zn^{2+} transport and deposition kinetics. The binding energies of Zn^{2+} with various carbonyl groups in the hard segments range from −0.48 to −0.59 eV, significantly less negative than Zn^{2+} with carboxyl (−1.03 eV) and sulfonate (−1.08 eV) groups in the soft segments. These results align with the ESP distributions and Zn^{2+} migration energy barriers, further confirming the synergistic structure–function mechanism in PUMA: hard segments provide mechanical robustness, whereas soft segments dominate Zn^{2+} transport regulation. The frontier orbital energy levels (HOMO–LUMO) further elucidated the electronic-structure origin of the soft segments' high affinity for Zn^{2+}. The polar-group-rich soft segments exhibit a significantly narrower bandgap (3.33 eV) than water (5.59 eV) and the polyurea–polyurethane hard segments (4.42 eV) (Figure 3e), indicating higher electronic polarizability and interfacial reactivity. This arises from strong interactions between the soft-segment polar groups and electron-deficient Zn^{2+}, facilitating Zn^{2+} migration and redistribution across the PUMA network. PUMA not only regulates Zn^{2+} solvation structure and transport behavior but also exhibits strong interfacial affinity toward the Zn anode: its binding energy on the Zn(002) surface is −0.73 eV, more negative than that on the Zn(101) surface (−0.61 eV) and far lower than the adsorption energy of H_2O on the Zn(002) surface (−0.25 eV) (Figure 3f). This thermodynamically favorable binding implies preferential adsorption of PUMA over water at the Zn anode interface, leading to effective displacement of interfacial water, enhanced PUMA/Zn interfacial adhesion, and suppression of parasitic water-derived side reactions.

To further elucidate how the PUMA layer regulates the interfacial microenvironment at the Zn anode, molecular dynamics (MD) simulations were conducted to quantitatively investigate the interfacial molecular distribution and the evolution of Zn^{2+} coordination environment. Without the PUMA layer (Figure S20a), water molecules densely adsorb onto the Zn surface, forming a compact hydration layer that directly contacts the Zn anode and thereby creating a highly active interface for water-induced side reactions. After introduction, the PUMA layer significantly suppresses side reactions via two synergistic mechanisms: (i) physically blocking direct electrolyte–Zn contact by occupying water adsorption sites and (ii) immobilizing water molecules through a dense H-bonding network. Radial distribution function (RDF) analysis further shows that PUMA increases the average interfacial Zn^{2+} population near the Zn electrode surface from 6.3 to 12.3 (Figures 3h,i and S20b,c), indicating enhanced interfacial Zn^{2+} enrichment and more favorable interfacial ion transport. Concurrently, the functional groups in PUMA competitively coordinate with Zn^{2+}, partially displacing water molecules (decreases from 5.68 to 5.38) and SO_4^{2-} (decreases from 0.32 to 0.19) from the primary solvation shell, thereby reconstructing the Zn^{2+} solvation structure [58]. This structural reorganization effectively weakens Zn^{2+}–water interaction, suppresses water decomposition, and optimizes Zn^{2+} diffusion and deposition behavior, ultimately improving electrode reaction kinetics and interfacial stability.

2.3 | Integrated SEI/PUMA Interface Induced by In Situ Electrochemical Reduction

The above theoretical calculations and simulations indicate that PUMA can synergistically regulate the Zn^{2+} solvation structure, interfacial microenvironment, and ion transport behavior through its soft and hard segments, enabling efficient interfacial stabilization. Nevertheless, during practical battery cycling, it remains unclear whether PUMA undergoes in situ chemical transformation at the Zn anode interface or influences the solid electrolyte interphase (SEI), key questions for further clarifying its long-term protection mechanism. Therefore, after electrochemical cycling, the outer PUMA layer was carefully removed and the exposed Zn anode surface was then systematically characterized.

15213773, 0, Downloaded from https://onlinelibrary.wiley.com/doi/10.1002/anie.7908002 by Li Dongdong - Guangxi University , Wiley Online Library on [24/10/2026]. See the Terms and Conditions (https://onlinelibrary.wiley.com/terms-and-conditions) on Wiley Online Library for rules of use; OA articles are governed by the applicable Creative Commons License

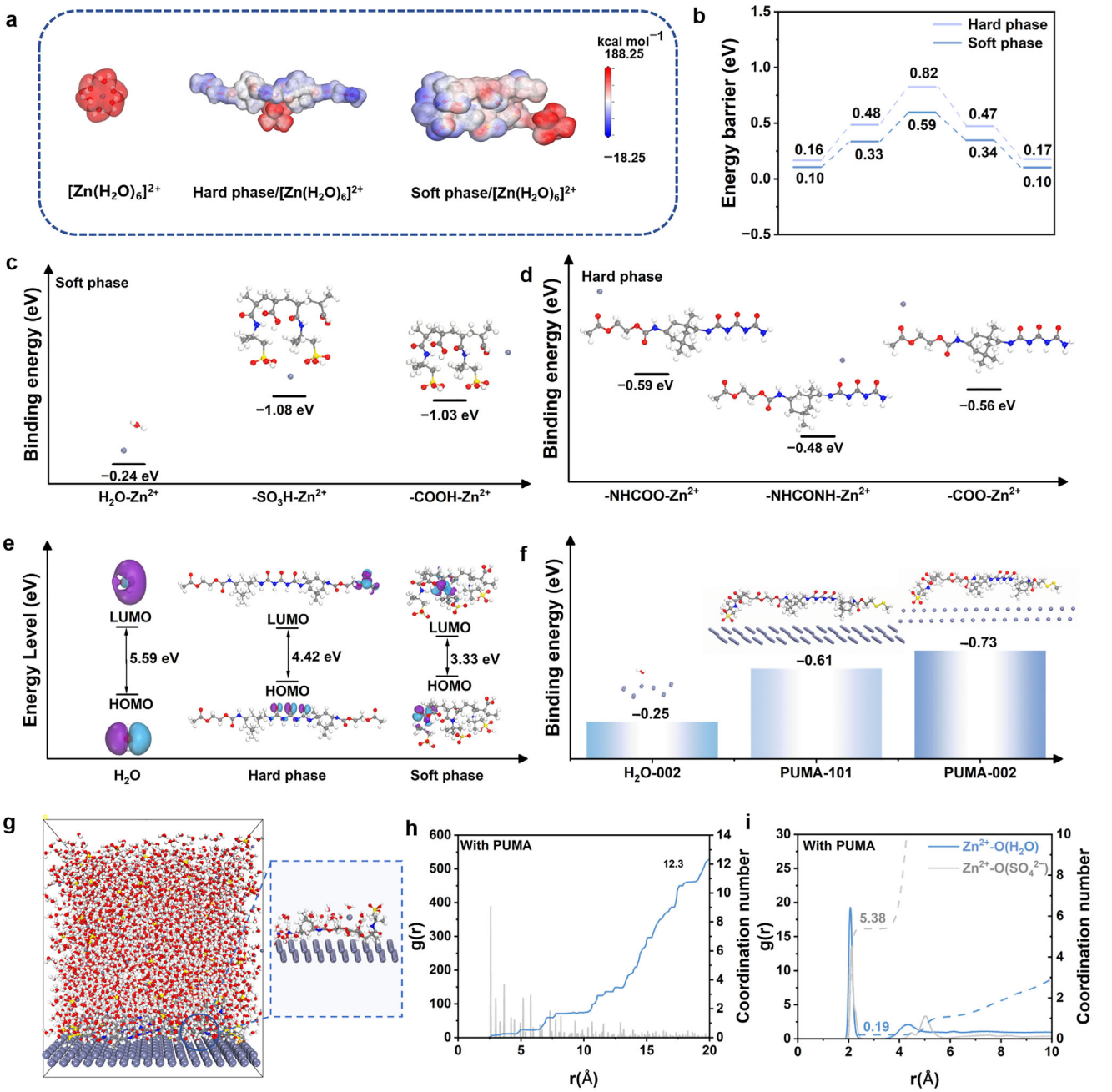


FIGURE 3 | (a) ESP maps of $[Zn(H_2O)_6]^{2+}$, hard segment/$[Zn(H_2O)_6]^{2+}$, and soft segment/$[Zn(H_2O)_6]^{2+}$. (b) Zn^{2+} migration energy barrier in the hard and soft segments. Binding energies of Zn^{2+} with different functional groups in the (c) soft and (d) hard segments. (e) HOMO–LUMO energy-level diagrams of H_2O, the hard segment, and the soft segment. (f) Binding energies of H_2O and PUMA on different Zn crystal facets. (g) MD simulation snapshot of the PUMA/Zn interface, with an enlarged view highlighting interfacial atomic arrangements. (h) RDFs of the system in the presence of PUMA, and (i) corresponding coordination numbers of Zn^{2+}−O (H_2O) and Zn^{2+}−O (SO_4^{2-}).

XPS depth profiling of the Zn anode interface after PUMA removal revealed the chemical composition and spatial distribution. Figure 4a shows depth-dependent S 2p spectra of the PUMA-derived Zn anode interface: the sulfur-containing species change markedly with etching depth. The S—O signal at 169.1 eV is primarily attributed to the sulfonic groups derived from AMPS and may also include a minor contribution from electrolyte sulfate; the S—S/C—S signal (164.5 eV) is mainly concentrated near the surface and decreases rapidly with etching depth, while the Zn—S/R—S—Zn signal (162.7 eV) intensifies significantly, demonstrating progressive enrichment of Zn—S-bonded sulfur-containing species toward the Zn substrate [50, 59, 60]. This inverse trend (i.e., S—S/C—S signal decreases while Zn—S signal increases with increasing etching depth) indicates that some of the dynamic S—S linkages in PUMA undergo sacrificial cleavage during electrochemical cycling and react in situ with the Zn anode to generate Zn—S species. To exclude other possible sulfur sources, an AMPS-free system using $Zn(OAc)_2$ electrolyte was examined (Figure S21). After cycling, the S 2p spectrum still shows Zn—S/R—Zn—S and residual S—S/C—S signals, while

15213773, 0, Downloaded from https://onlinelibrary.wiley.com/doi/10.1002/anie.7908002 by Li Dongdong - Guangxi University , Wiley Online Library on [24/10/2026]. See the Terms and Conditions (https://onlinelibrary.wiley.com/terms-and-conditions) on Wiley Online Library for rules of use; OA articles are governed by the applicable Creative Commons License

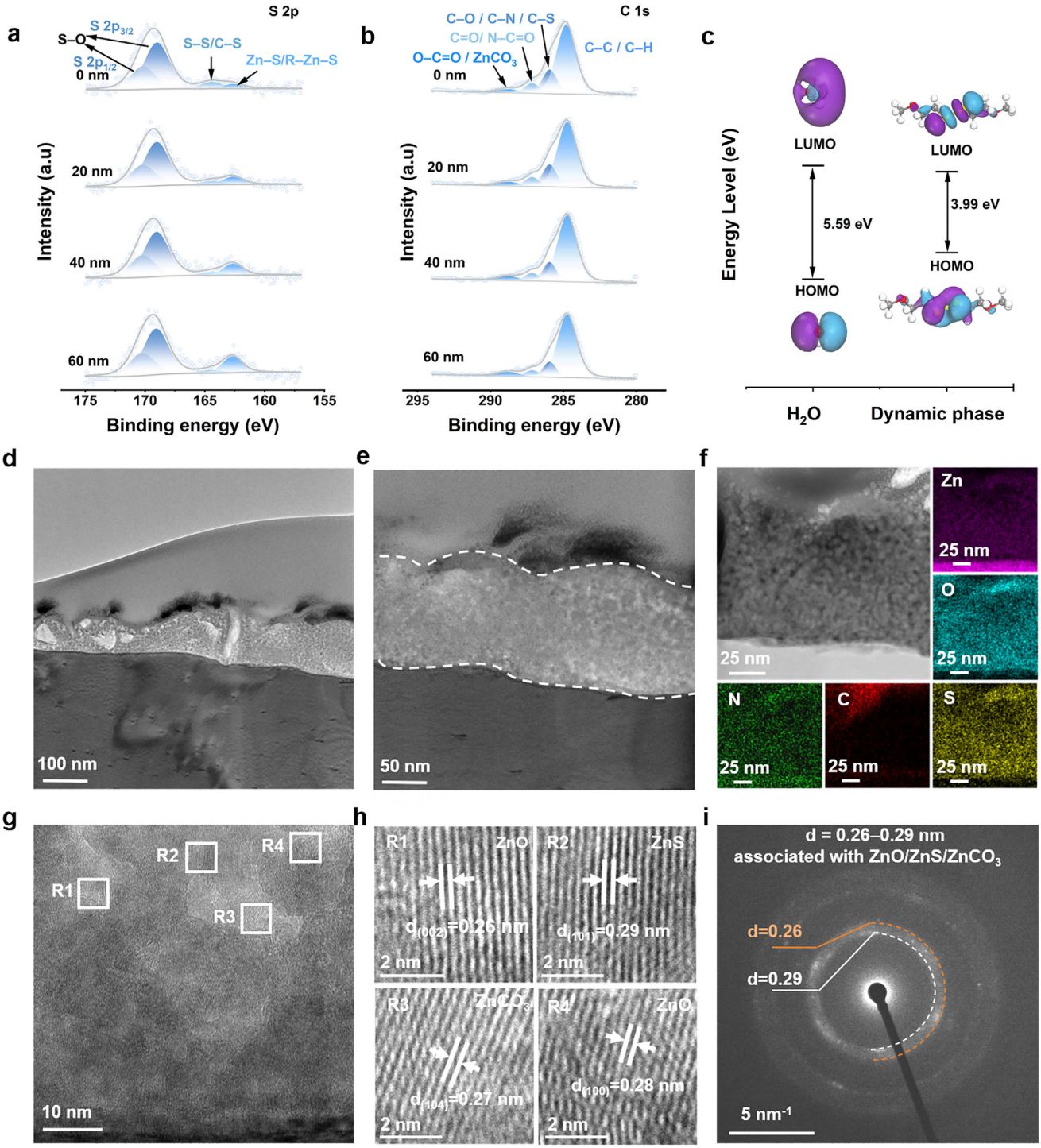


FIGURE 4 | (a, b) S 2p and C 1s XPS depth-profiling spectra of the residual interfacial layer on the Zn electrode after removal of the outer PUMA gel layer. (c) HOMO–LUMO energy levels of H_2O and the dynamic S—S segment. (d, e) Cross-sectional TEM images of cycled Zn anodes after removal of the outer PUMA gel layer. The continuous covering layer at the top of the TEM images is the carbon protective layer deposited during FIB sample preparation. (f) HAADF–STEM image and the corresponding elemental mappings of Zn, O, N, C, and S. (g) HRTEM image of the interfacial region. (h) Enlarged lattice-fringe images of selected regions R1–R4, showing interplanar spacings matching those of ZnO, ZnS, and $ZnCO_3$-related inorganic species. (i) SAED pattern of the interfacial layer, showing broad diffraction rings corresponding to interplanar spacings of 0.26–0.29 nm.

15213773, 0, Downloaded from https://onlinelibrary.wiley.com/doi/10.1002/anie.7908002 by Li Dongdong - Guangxi University , Wiley Online Library on [24/10/2026]. See the Terms and Conditions (https://onlinelibrary.wiley.com/terms-and-conditions) on Wiley Online Library for rules of use; OA articles are governed by the applicable Creative Commons License

no obvious S—O species are observed. These results support that the interfacial Zn—S species mainly originate from the electrochemical conversion of the disulfide units in PU–SS–HEMA. The HOMO–LUMO calculations (Figure 4c) further reveal that the dynamic S—S segment exhibits a narrower energy gap (3.99 eV) than that of H_2O (5.59 eV), directly supporting its lower electronic excitation barrier and thermodynamic tendency to participate in interfacial electrochemical reactions. In addition, the C 1s spectrum (Figure 4b) shows four interfacial components: C—C/C—H (284.8 eV), C—O/C—N/C—S (285.9 eV), C═O/N—C═O (287.2 eV), and O—C═O/$ZnCO_3$-related species (288.8 eV) components in the interfacial region [61, 62], indicating coexistence of PUMA-derived organic residues and carbonate-based inorganic species on the cycled Zn anode surface. Notably, as Ar^+ etching depth increases from 0 to 60 nm, the organic carbon-related signals gradually decrease, whereas the O—C═O/$ZnCO_3$-related component progressively increases, indicating that the inorganic carbonate component is enriched in the inner region of the SEI film. Collectively, these results demonstrate that the PUMA not only firmly adheres to the Zn anode surface via in situ polymerization to build a compact interfacial film, but also enables the dynamic S—S segments to engage in interfacial transformation upon cycling. Such behavior triggers the in situ formation of an integrated SEI/PUMA architecture on the Zn anode, thereby remarkably enhancing the bonding stability between the PUMA layer and the Zn substrate.

Transmission electron microscopy (TEM), high-angle annular dark-field scanning transmission electron microscopy (HAADF–STEM), and EDS were employed to characterize the cross-section of the Zn anode after peeling off the outer PUMA layer, enabling direct investigation of the microstructure and compositional distribution within the PUMA-derived SEI layer. The cross-sectional TEM image (Figure 4d) shows a continuous SEI film covering the Zn anode surface, with locally distributed pores. This structural feature arises from the significant modulus mismatch between the inorganic particles (or brittle components) and the organic components within the SEI layer, which may cause localized fracture or particle detachment under ion-beam bombardment and mechanical stress during focused ion beam (FIB) cross-sectional sample preparation [62]. The high-magnification image (Figure 4e) further shows that the PUMA-derived SEI film extends continuously along the Zn anode surface (the topmost continuous layer is the carbon protective coating deposited during FIB sample preparation) and maintains intimate, gap-free contact with the Zn substrate, indicating excellent interfacial conformity and structural stability. HAADF–STEM/EDS mapping reveals that the SEI layer is rich in O, S, and N; the C signal is obscured by the carbon protective layer and thus does not reflect the intrinsic carbon distribution, while the strong Zn signal is mainly concentrated in the underlying Zn substrate (Figure 4f). Combined with the enhanced Zn—S/R—S—Zn signal in XPS (Figure 4a), these results further confirm that PUMA participates in interfacial reactions and in situ constructs an integrated organic–inorganic hybrid SEI.

High-resolution TEM shows that the organic/inorganic hybrid SEI consists of an amorphous matrix with embedded ordered nanocrystallites (Figure 4g). In the selected regions R1–R4, well-defined lattice fringes were resolved with interplanar spacings of 0.26, 0.29, 0.27, and 0.28 nm, corresponding to ZnO (002), ZnS (101), $ZnCO_3$ (104), and ZnO (100), respectively (Figure 4h) [62, 63]. Meanwhile, the selected-area electron diffraction (SAED) pattern displays broadened diffuse diffraction rings, which correspond to interplanar spacings of approximately 0.26–0.29 nm (Figure 4i). Based on the above analysis, it can be confirmed that a hybrid SEI comprising PUMA-related organic residues and Zn-containing inorganic species forms during cycling. The inorganic species exhibit a gradient distribution, enriched near the Zn substrate, whereas the PUMA-related organic components were enriched in the outer region. This SEI ultimately merges with the PUMA layer, creating a stable integrated SEI/PUMA interface and thereby achieving strong interfacial anchoring of the PUMA layer.

2.4 | Interfacial Regulatory Effects

The regulatory effects of PUMA on interfacial side reactions and Zn deposition behavior were systematically investigated. Linear sweep voltammetry (LSV) (Figure 5a) shows that PUMA@Zn exhibits a significantly higher hydrogen evolution overpotential than Bare Zn, confirming strong HER suppression by the PUMA layer [64]. Tafel polarization (Figure 5b) shows that the corrosion current density of PUMA@Zn is significantly lower than that of Bare Zn, indicating that the PUMA layer effectively blocks direct Zn anode-electrolyte contact, thereby markedly suppressing Zn corrosion [65]. Chronoamperometry (CA) was performed to characterize Zn^{2+} diffusion and deposition behavior. As shown in Figure 5c, the current density of Bare Zn continuously increases with time, suggesting two-dimensional lateral Zn^{2+} diffusion that readily induces nonuniform nucleation and dendrite growth [66]. In contrast, the current response of the PUMA@Zn rapidly reaches a steady state within a short period, indicating that the PUMA layer effectively suppresses disordered two-dimensional diffusion and thereby guides uniform Zn nucleation and dense deposition [67]. To further clarify the evolution of interfacial kinetics during Zn deposition, progressive EIS coupled with DRT analysis was performed at cumulative Zn deposition capacities of 0–1.0 mAh cm^{-2} (Figure S22) [68, 69]. For Bare Zn, the dominant relaxation time (τ_{peak}) sharply shifts from $\sim 9.9 \times 10^{-3}$ s to 8–12 s after Zn deposition, indicating the rapid emergence of slow interfacial processes. In contrast, PUMA@Zn exhibits only a gradual shift from $\sim 4.6 \times 10^{-3}$ to 4.3×10^{-2} s, indicating markedly enhanced stability of the interfacial kinetic response throughout Zn electrodeposition.

In the electrolyte, Zn^{2+} mainly exists as $[Zn(H_2O)_6]^{2+}$, and its desolvation behavior governs Zn deposition kinetics [70, 71]. Arrhenius fitting (Figures 5d and S23) shows a lower apparent interfacial activation energy for PUMA@Zn (34.4 kJ mol^{-1}) than for Bare Zn (41.2 kJ mol^{-1}). This is consistent with the lower interfacial impedance measured by EIS (Figure S24), confirming that the PUMA layer effectively reduces the desolvation energy barrier and thereby accelerates interfacial desolvation kinetics [72]. Ion transport regulation by PUMA was evaluated via ionic conductivity and the Zn^{2+} transference number. As shown in Figures 5e and S7, PUMA exhibits an ionic conductivity of 31.8 mS cm^{-1}, much higher than that of the 2 M $ZnSO_4$ electrolyte (12.1 mS cm^{-1}). This enhancement arises from the continuous and efficient Zn^{2+} transport pathways provided by the flexible soft chains, together with the significantly promoted desolvation

15213773, 0, Downloaded from https://onlinelibrary.wiley.com/doi/10.1002/anie.7908002 by Li Dongdong - Guangxi University , Wiley Online Library on [24/10/2026]. See the Terms and Conditions (https://onlinelibrary.wiley.com/terms-and-conditions) on Wiley Online Library for rules of use; OA articles are governed by the applicable Creative Commons License

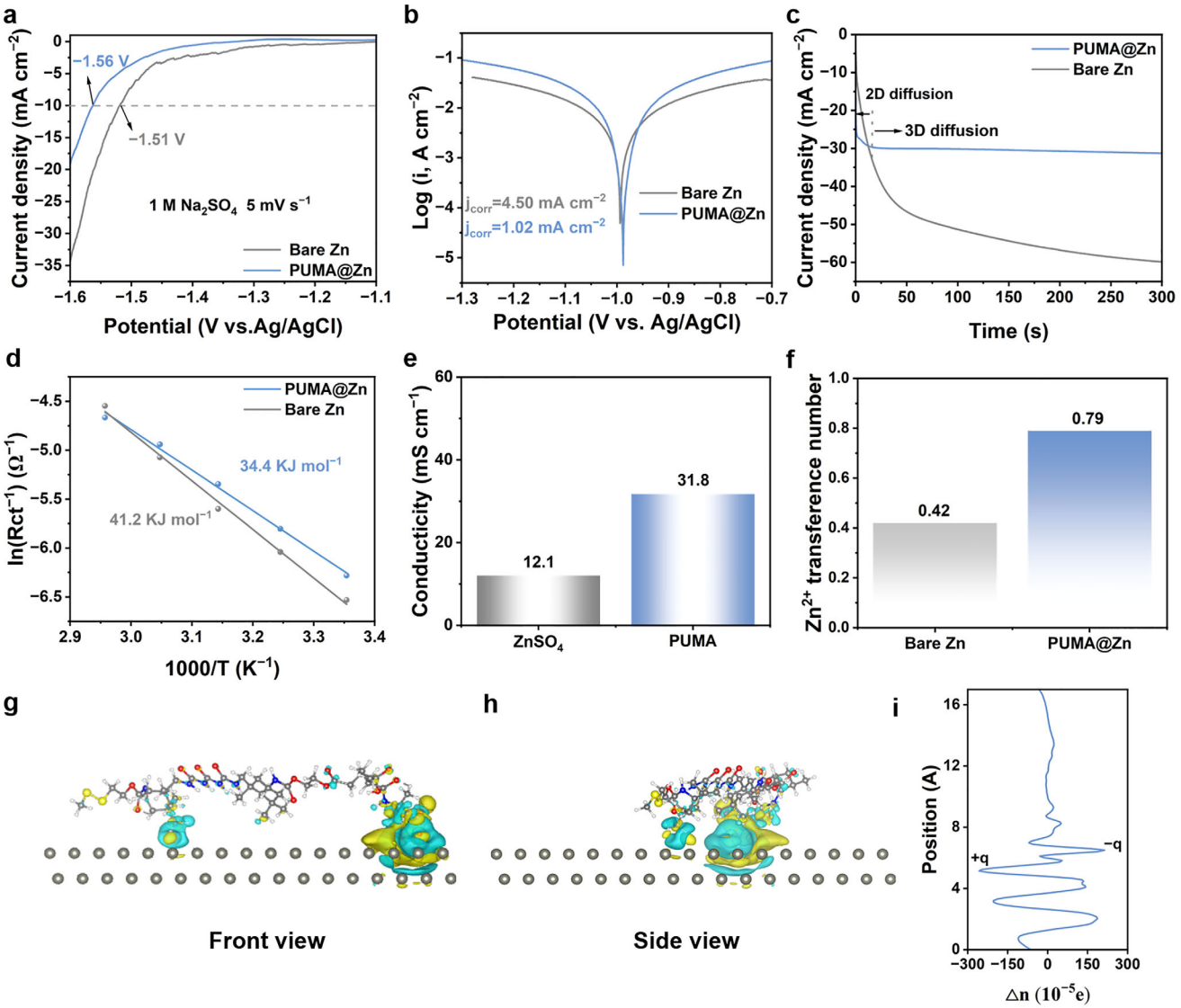


FIGURE 5 | (a) LSV curves, (b) Tafel polarization curves, and (c) chronoamperometric curves of Bare Zn and PUMA@Zn electrodes. (d) Arrhenius plots and the calculated desolvation activation energies of Bare Zn and PUMA@Zn. (e) Ionic conductivity and (f) Zn^{2+} transference number. Charge-density difference of PUMA adsorbed on the Zn surface: (g) front view and (h) side view, with the cyan and yellow regions indicating electron depletion and accumulation, respectively. (i) Corresponding planar-averaged charge-density-difference profile along the z-axis.

kinetics enabled by the strongly polar groups. The Zn^{2+} transference number of PUMA reaches 0.79 (Figures 5f and S25), significantly higher than that of the 2 M $ZnSO_4$ electrolyte (0.42). This highly selective Zn^{2+} transport capability originates from a locally anion-rich microenvironment constructed by carboxyl and sulfonic acid groups within the PUMA soft segments, effectively suppressing concentration polarization and promoting dense, dendrite-free Zn deposition. In addition, upon PUMA incorporation, differential charge density analysis (Figure 5g,h) reveals directional electron transfer from the Zn substrate (cyan) to the PUMA molecules (yellow), establishing an interfacial built-in electric field (Figure 5i) with a positive charge on the Zn side and a negative charge on the PUMA side. This electric field provides a driving force for Zn^{2+} migration along its direction, thereby buffering Zn^{2+} transport and homogenizing Zn^{2+} flux to suppress dendrite growth [73]. The synergistic interplay of the above interfacial electronic regulation, a high Zn^{2+} transference number, and a low desolvation energy barrier collectively enables the PUMA layer to accelerate Zn^{2+} transport kinetics and optimize interfacial mass-transfer behavior.

In addition, to directly assess interfacial stability, Bare Zn and PUMA@Zn were immersed in 2 M $ZnSO_4$ electrolyte for 7 days and characterized by SEM and XRD. SEM images (Figure S26) reveal pronounced corrosion and a highly rough, nonuniform surface morphology on the Bare Zn surface. In contrast, after removal of the PUMA layer, the PUMA@Zn remains a relatively smooth and uniform surface morphology, with no discernible corrosion features or by-product accumulation. Consistent with these SEM observations, XRD analysis (Figure S27) clearly confirms the formation of $Zn_4SO_4(OH)_6{\cdot}xH_2O$ (ZHS) by-products on the Bare Zn surface [74], whereas no identifiable by-product diffraction peaks were detected on the PUMA@Zn surface. These results demonstrate that the PUMA layer confers excellent

15213773, 0, Downloaded from https://onlinelibrary.wiley.com/doi/10.1002/anie.7908002 by Li Dongdong - Guangxi University , Wiley Online Library on [24/10/2026]. See the Terms and Conditions (https://onlinelibrary.wiley.com/terms-and-conditions) on Wiley Online Library for rules of use; OA articles are governed by the applicable Creative Commons License

corrosion resistance and significantly enhances Zn anode stability in aqueous electrolyte.

2.5 | Electrochemical Performance of the PUMA@Zn Anode

Zn//Zn symmetric cells and Zn//Cu half-cells were used to evaluate Zn plating/stripping reversibility. As shown in Figure 6a, the PUMA@Zn electrode maintains stable voltage polarization across a wide current density range (1–30 mA cm^{-2}), with full and rapid recovery upon current reduction; in contrast, Bare Zn suffers severe voltage fluctuations and eventual short-circuiting at high current densities, indicating that the integrated SEI/PUMA interface can effectively stabilize high-rate Zn plating/stripping. To further elucidate the thermodynamic origin of the distinct Zn deposition behaviors, galvanostatic deposition and CV measurements were performed to quantify the Zn nucleation overpotential. According to classical nucleation theory, the critical nucleation radius and nucleation overpotential satisfy the following relationship [75, 76]:

$$r_{crit} = \frac{2\gamma V_m}{nF \mid \eta \mid}$$

where, r_{crit} is the critical nucleation radius, γ is the Zn/electrolyte interfacial free energy, F is the Faraday constant, V_m is the molar volume of metallic Zn, n is the number of electrons transferred in the Zn^{2+}/Zn deposition reaction ($n = 2$), and η is the deposition nucleation overpotential. Clearly, a higher nucleation overpotential significantly lowers the critical nucleation size, which is a thermodynamic prerequisite for achieving uniform Zn deposition. As shown in Figure 6b, the nucleation overpotential of Bare Zn was only 33 mV, indicating a low Zn^{2+} nucleation energy barrier; this facilitates rapid Zn^{2+} deposition at surface defects and thereby promotes dendrite formation. In contrast, the nucleation overpotential of PUMA@Zn increased to 48 mV, highly consistent with the CV results showing a 23 mV negative shift in the Zn^{2+} nucleation overpotential relative to Bare Zn (Figure S28). A higher nucleation overpotential thermodynamically favors the formation of high-density, small nuclei, thereby facilitating subsequent uniform Zn deposition [77–79]. Therefore, the integrated SEI/PUMA interface can effectively optimize Zn deposition by regulating Zn nucleation.

Zn//Zn symmetric cells were employed to evaluate cycling stability. At 1 mA cm^{-2} and 0.5 mAh cm^{-2}, as well as 5 mA cm^{-2} and 2.5 mAh cm^{-2}, Bare Zn failed within 150 and 100 h, respectively, due to uncontrolled dendrite growth and interfacial side reactions. In contrast, PUMA@Zn stably cycled for 5080 and 1300 h under the same conditions with stable voltage polarization (Figures 6c and S29), demonstrating highly reversible Zn plating/stripping. Even at 10 mA cm^{-2} and 5 mAh cm^{-2}, PUMA@Zn maintained stable cycling for over 800 h, far exceeding Bare Zn (50 h) (Figure 6d), confirming the enhanced cycling stability enabled by the integrated SEI/PUMA interface. Intermittent cycling tests were further conducted at 10 mA cm^{-2} and 5 mAh cm^{-2} with 30 h open-circuit rest periods to evaluate corrosion resistance during resting. As shown in Figure 6e, Bare Zn failed within 100 h due to HER and corrosion, whereas PUMA@Zn remained stable for over 1000 h. These results confirm that PUMA suppresses dendrite growth during cycling and interfacial side reactions during resting, thereby improving Zn anode operational reliability. Depth of discharge (DOD) directly affects Zn anode utilization rate and thus determines the battery's overall energy density [80]. PUMA@Zn achieved stable cycling for over 470 h at an ultrahigh DOD of 80%, whereas Bare Zn short-circuited after only 67 h (Figure S30), demonstrating the strong protective capability of the integrated SEI/PUMA interface under extreme conditions. Zn plating/stripping reversibility was further evaluated by Coulombic efficiency (CE). As shown in Figure 6f, the Bare Zn//Cu cell exhibits highly unstable CE at 1 mA cm^{-2} and 0.5 mAh cm^{-2}, rapidly declining due to irreversible active-material loss caused by side reactions and dead-Zn accumulation [81]. In contrast, the PUMA@Zn//Cu cell cycled stably for over 4000 cycles with an average CE of 99.64%. Its higher voltage polarization than Bare Zn//Cu (Figure S31) is consistent with the increased nucleation overpotential discussed above, further indicating that PUMA optimizes Zn nucleation and maintains long-term Zn plating/stripping reversibility.

Furthermore, single-component coatings were compared to verify the necessity of combining AA and AMPS. At 1 mA cm^{-2} and 0.5 mAh cm^{-2}, the optimal single-component coating cycled for 2900 h, whereas the combined carboxyl and sulfonic acid groups enhanced PUMA's mechanical strength and ion transport, enabling over 5000 h of cycling (Figure S32). Performance comparisons (Figure 6g and Table S2) further show that PUMA@Zn ranks among the top-performing Zn anodes under both low—and high-rate conditions.

SEM and three-dimensional confocal laser scanning microscopy (3D CLSM) were employed to characterize the Zn anode morphology after cycling. Figure 7a,b show highly nonuniform Zn deposition on the Bare Zn surface, characterized by abundant loose, flake-like dendrites and surface height fluctuations reaching 56.5 μm. This rough surface aggravates interfacial side reactions and "dead Zn" accumulation, thereby increasing polarization and lowering CE. In sharp contrast, the PUMA@Zn electrode maintains a smooth, dendrite-free surface after cycling, with surface height fluctuations reduced to approximately 38.2 μm (Figure 7c,d), indicating substantially enhanced Zn deposition uniformity. XRD analysis after cycling shows distinct ZHS by-product signals on the Bare Zn surface, whereas nearly no by-product signals were detected on the PUMA@Zn surface (Figure S33), demonstrating effective suppression of interfacial side reactions. Collectively, the PUMA layer markedly optimizes Zn deposition and suppresses side reactions by synergistically improving Zn^{2+} transport, regulating the interfacial water environment, and optimizing Zn nucleation. In addition, FTIR and cross-sectional SEM (Figures S34 and S35) further confirm that both the functional groups of PUMA and its interfacial structure remain unchanged after cycling, demonstrating exceptional stability.

In situ optical microscopy directly visualized Zn deposition behavior (Figure 7e,g). At 10 mA cm^{-2}, Bare Zn developed uneven tip-like protrusions within 10 min, which progressively evolved into sharp, disordered dendrites after 60 min. In contrast, PUMA@Zn maintained a flat, dendrite-free surface throughout deposition, indicating that PUMA promotes uniform Zn nucleation and transport. SEM images of the pristine electrodes

15213773, 0, Downloaded from https://onlinelibrary.wiley.com/doi/10.1002/anie.7908002 by Li Dongdong - Guangxi University , Wiley Online Library on [24/10/2026]. See the Terms and Conditions (https://onlinelibrary.wiley.com/terms-and-conditions) on Wiley Online Library for rules of use; OA articles are governed by the applicable Creative Commons License

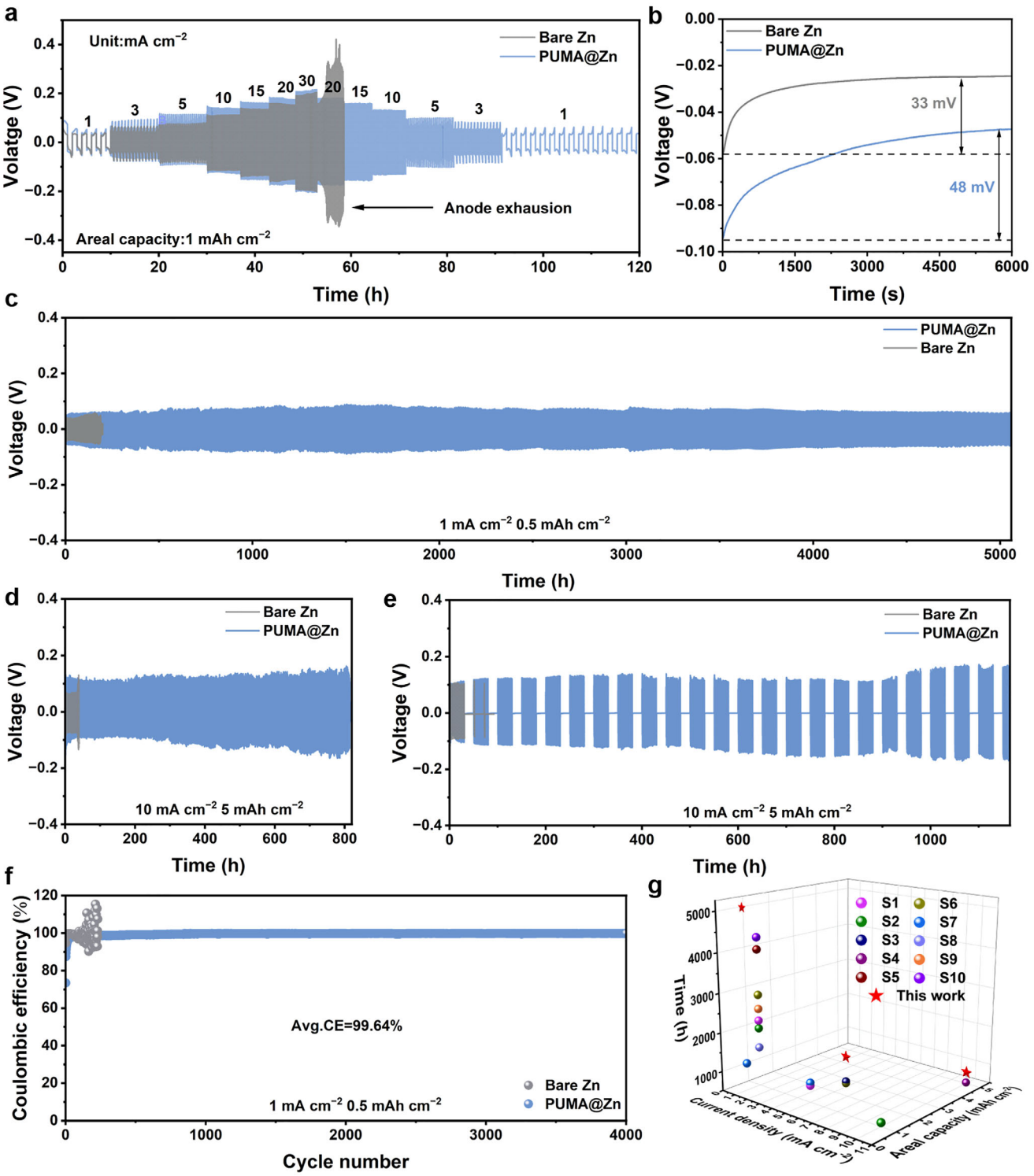


FIGURE 6 | (a) Rate performance of different electrodes. (b) Nucleation overpotential curves of different electrodes. Long-term cycling stability of Bare Zn and PUMA@Zn anodes at (c) 1 mA cm^{-2} and 0.5 mAh cm^{-2} and (d) 10 mA cm^{-2} and 5 mAh cm^{-2}. (e) Intermittent cycling stability of symmetric cells at 10 mA cm^{-2}, 5 mAh cm^{-2} with 30 h open-circuit rest periods between cycles. (f) Coulombic efficiency of Zn//Cu cells at 1 mA cm^{-2} and 0.5 mAh cm^{-2}. (g) Performance comparison of PUMA@Zn with previously reported Zn anode protective layers.

(Figure S36) further reveal that Bare Zn contains scratches and microprotrusions that distort the local electric field and trigger dendrite growth, whereas in situ polymerization of PUMA produces a smooth, uniform surface that homogenizes the interfacial electric field and facilitates uniform Zn deposition [82]. COMSOL Multiphysics simulations demonstrate that microprotrusions on the Bare Zn surface induce a pronounced "tip effect," amplifying interfacial potential and current density at the protrusion tips. This concentrates Zn^{2+} flux and promotes preferential reduction at the protrusion tips, directly triggering

15213773, 0, Downloaded from https://onlinelibrary.wiley.com/doi/10.1002/anie.7908002 by Li Dongdong - Guangxi University , Wiley Online Library on [24/10/2026]. See the Terms and Conditions (https://onlinelibrary.wiley.com/terms-and-conditions) on Wiley Online Library for rules of use; OA articles are governed by the applicable Creative Commons License

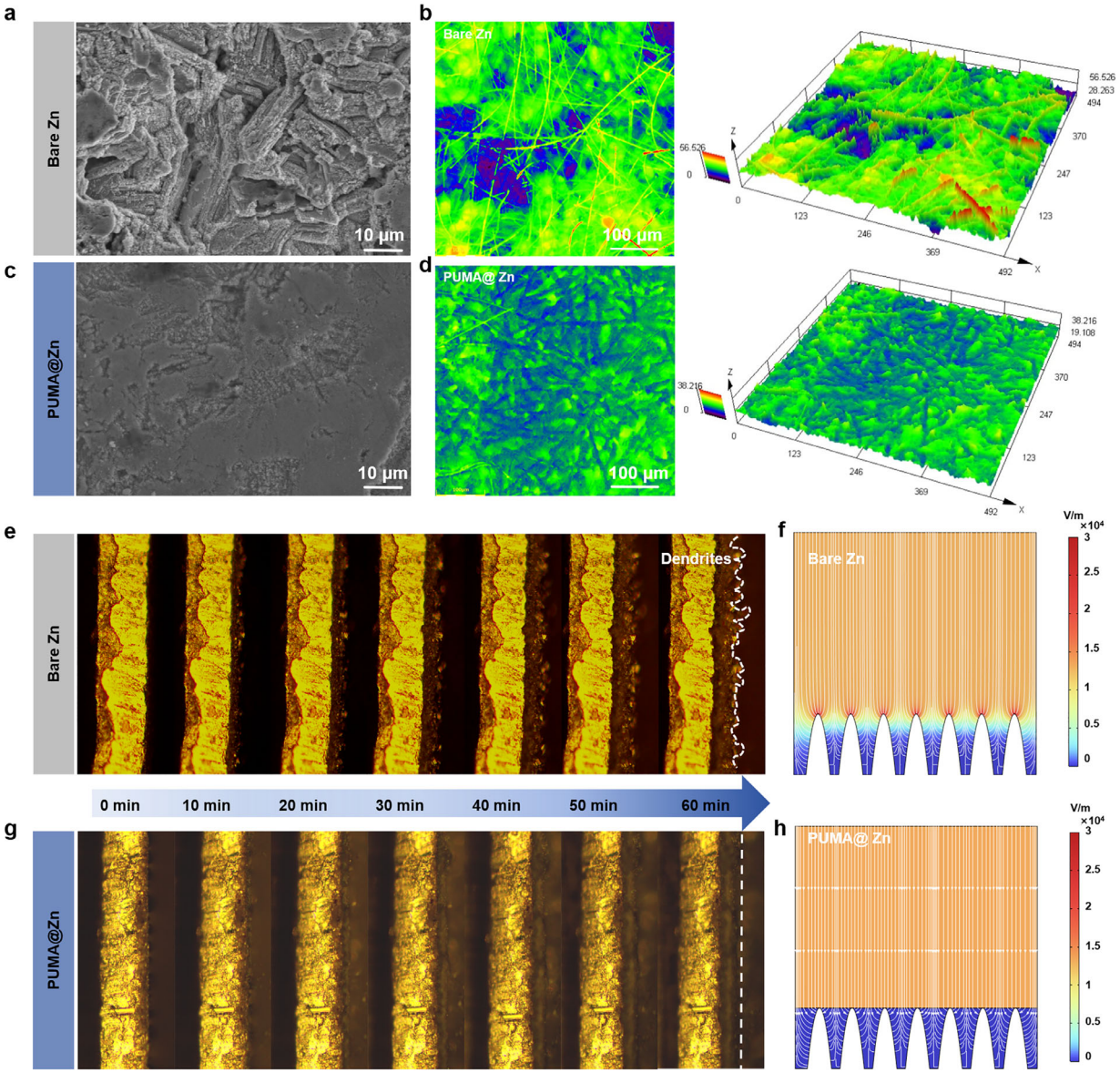


FIGURE 7 | (a, c) Surface SEM images and (b, d) 3D CLSM images of Bare Zn and PUMA@Zn anodes after 50 cycles at 10 mA cm^{-2} and 5 mAh cm^{-2}. In situ optical microscopy images of Zn deposition on (e) Bare Zn and (g) PUMA@Zn at 10 mA cm^{-2}. COMSOL simulations of interfacial electric-field distributions for (f) Bare Zn and (h) PUMA@Zn.

dendrite growth (Figures 7f and S37a) [83]. In contrast, the PUMA layer renders equipotential lines highly parallel (Figure 7h) and significantly homogenizes surface current distribution (Figure S37b), confirming its ability to suppress tip-induced electric field distortion and establish a spatially uniform interfacial electrochemical environment, thereby redirecting disordered, localized Zn deposition toward stable, two-dimensional uniform growth [66].

2.6 | Electrochemical Performance of Full Cells

PUMA@Zn//I_2 full cells with high-areal-loading iodine cathodes were assembled to evaluate the interfacial regulation and practical applicability of PUMA. As shown in Figure 8a, negatively charged sites in PUMA electrostatically repel I_3^-/I_5^- polyiodide anions, limiting their migration toward the Zn anode and mitigating iodine-induced corrosion. CV analysis (Figure 8b) shows a smaller redox peak separation and higher peak currents for PUMA@Zn//I_2 than Bare Zn//I_2, indicating accelerated redox kinetics. This improvement arises from the dual role of PUMA in stabilizing the Zn anode and suppressing polyiodide shuttling, thereby reducing polarization and improving active-material utilization. EIS results (Figure 8c) further reveal a lower charge-transfer resistance, indicating improved interfacial compatibility. Self-discharge remains a major challenge for practical Zn–I_2 batteries [3]. After charging to 1.6 V and resting for 24 h, the PUMA@Zn//I_2 cell retains 95.9% of its initial capacity, compared with 88.4% for Bare Zn//I_2 (Figure S38), confirming that PUMA suppresses self-discharge by inhibiting polyiodide shuttling and Zn-anode side reactions.

H-type permeation and static Zn immersion tests were performed to evaluate PUMA's suppression of polyiodide migration and Zn

15213773, 0, Downloaded from https://onlinelibrary.wiley.com/doi/10.1002/anie.7908002 by Li Dongdong - Guangxi University , Wiley Online Library on [24/10/2026]. See the Terms and Conditions (https://onlinelibrary.wiley.com/terms-and-conditions) on Wiley Online Library for rules of use; OA articles are governed by the applicable Creative Commons License

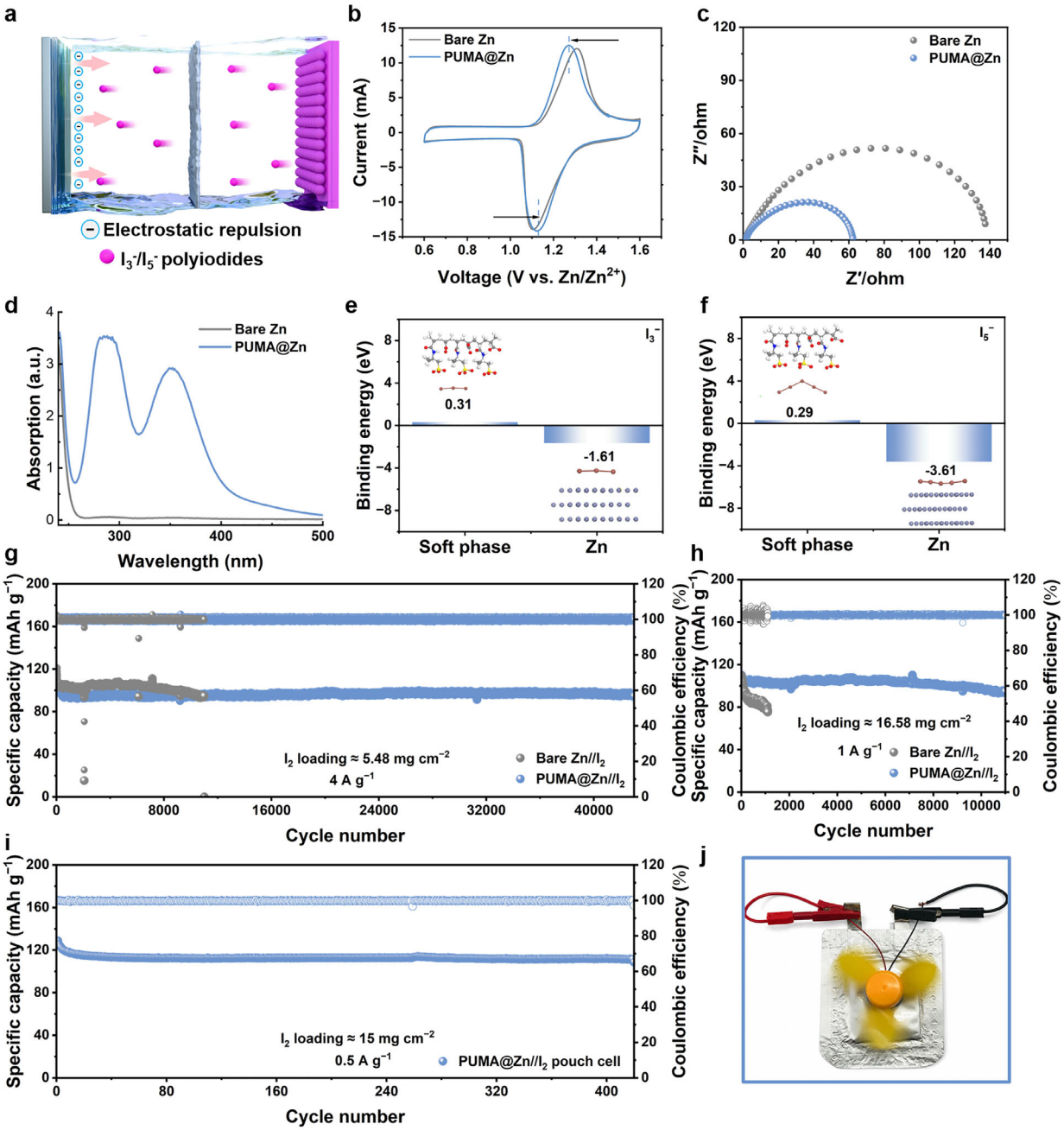


FIGURE 8 | (a) Schematic illustration of the electrostatic repulsion of I_3^-/I_5^- by PUMA layer. (b) CV curves and (c) EIS spectra of Bare Zn//I_2 and PUMA@Zn//I_2 cells. (d) UV–vis spectra of 2 mM polyiodide solutions after immersion of Bare Zn and PUMA@Zn for 72 h. (e, f) Calculated binding energies of I_3^- and I_5^- with the PUMA soft segment and Zn surface. (g, h) Cycling performance of Bare Zn//I_2 and PUMA@Zn//I_2 cells at I_2 loadings of 5.48 and 16.58 mg cm^{-2} at 4 and 1 A g^{-1}, respectively. (i) Cycling performance of the PUMA@Zn//I_2 pouch cell. (j) Photograph of the pouch cell powering a miniature fan.

corrosion. I_3^- rapidly crossed the pristine glass-fiber separator within 30 min, whereas no visible diffusion occurred across the PUMA–GF separator even after 6 h (Figure S39), demonstrating effective polyiodide blocking by the polyanionic network. In the immersion test (Figure S40), the I_3^- solution containing Bare Zn faded from yellow to nearly colorless within 72 h, while that containing PUMA@Zn remained dark yellow, confirming that PUMA effectively prevents direct I_3^-–Zn contact and suppresses polyiodide-induced corrosion [84]. Corresponding UV–vis spectra (Figure 8d) show that the characteristic I_3^- peaks at 288 and 350 nm remain nearly unchanged after 72 h with PUMA@Zn but almost disappear with Bare Zn, further confirming that PUMA suppresses polyiodide diffusion and polyiodide-induced Zn corrosion [22]. DFT calculations further support the anti-shuttle mechanism. Using deprotonated carboxyl and sulfonic acid models, the binding energies with I_3^- and I_5^- are 0.31 and 0.29 eV, respectively, indicating repulsion, whereas the corresponding binding energies on Bare Zn are −1.61 and −3.61 eV, respectively (Figure 8e,f), reflecting strong favorable adsorption. These results confirm that the negatively charged PUMA soft segments repel polyiodide anions, reducing their accumulation on Zn and suppressing polyiodide-induced side reactions.

15213773, 0, Downloaded from https://onlinelibrary.wiley.com/doi/10.1002/anie.7908002 by Li Dongdong - Guangxi University , Wiley Online Library on [24/10/2026]. See the Terms and Conditions (https://onlinelibrary.wiley.com/terms-and-conditions) on Wiley Online Library for rules of use; OA articles are governed by the applicable Creative Commons License

Based on the combined effects of interfacial stabilization and polyiodide shuttle suppression, PUMA markedly improves Zn–I_2 cycling stability. At an iodine loading of 5.48 mg cm^{-2}, Bare Zn//I_2 shows rapid capacity decay after 1800 cycles, whereas PUMA@Zn//I_2 cycles stably for over 43 000 cycles (Figure 8g). Nearly identical first-cycle discharge capacities (Figure S41) indicate that PUMA does not hinder the electrochemical reaction. After 1000 cycles at 4 A g^{-1}, Bare Zn becomes severely roughened with obvious corrosion and by-product deposition, whereas PUMA@Zn remains smooth and compact (Figure S42). Consistently, the iodine content on PUMA@Zn is only 0.079 at.%, much lower than that on Bare Zn (0.29 at.%), confirming effective suppression of polyiodide shuttling. Even at an ultra-high iodine loading of 16.58 mg cm^{-2}, PUMA@Zn//I_2 operates stably for over 11 000 cycles at 1 A g^{-1} (Figures 8h and S43). Under more demanding conditions with a 15 μm-thick Zn foil, an I_2 loading of 23.5 mg cm^{-2}, and an N/P ratio of 2.6, PUMA@Zn//I_2 maintained stable cycling for over 2500 cycles at 1 A g^{-1}, whereas Bare Zn//I_2 exhibited pronounced capacity decay (Figure S44a). The corresponding capacity–voltage profiles further confirm that PUMA@Zn||I_2 maintains stable electrochemical behavior during prolonged cycling (Figure S44b,c). Moreover, a PUMA@Zn//I_2 pouch cell with an iodine loading of 15 mg cm^{-2} operates for over 400 cycles at 0.5 A g^{-1} and powers a miniature fan, demonstrating practical potential (Figure 8i,j).

To evaluate cathode compatibility, Zn//MnO_2 full cells were assembled using conventionally synthesized MnO_2 [85] and a 2 M $ZnSO_4$ + 0.1 M MnSO4 electrolyte, with XRD and SEM confirming successful MnO_2 synthesis (Figure S45). CV reveals similar redox peak positions for the PUMA@Zn//MnO_2 and Bare Zn//MnO_2 cells (Figure S46a), indicating that the PUMA layer does not affect the electrochemical reactions of the MnO_2 cathode. Moreover, the PUMA@Zn//MnO_2 cell exhibits smaller redox peak separation and higher peak currents, evidencing diminished cell polarization and accelerated redox kinetics [38, 86]. EIS shows a significantly lower charge-transfer resistance for the PUMA@Zn//MnO_2 cell (Figure S46b), indicating faster interfacial charge transfer. After 24 h of rest, the PUMA@Zn//MnO_2 cell retains 92.9% of its initial capacity, compared with 86.1% for Bare Zn//MnO_2 (Figure S47), confirming suppressed Zn-anode side reactions and improved open-circuit stability. At 1 A g^{-1}, Bare Zn//MnO_2 delivers an initial capacity of 160 mAh g^{-1} but retains only 50% after 1000 cycles, whereas PUMA@Zn//MnO_2 delivers 200 mAh g^{-1} and retains 85% after 1600 cycles (Figure S48), demonstrating superior long-term cycling stability. Collectively, these results demonstrate the broad applicability of the integrated SEI/PUMA interface for stabilizing Zn anodes in different aqueous battery systems.

3 | Conclusion

This study develops an integrated SEI/PUMA interface on Zn through molecular design and in situ electrochemical reduction, combining mechanical robustness, rapid Zn^{2+} transport, and interfacial stability. In the polyurea–polyurethane hard segments, octuple H-bonds, Zn^{2+} coordination, and dynamic S–S bonds form a multilevel energy-dissipation network that provides fatigue-resistant deformability, hot-press reprocessability, and suppression of side reactions. The polyanionic soft segments provide continuous ion-transport pathways and regulate the Zn^{2+} solvation sheath to accelerate deposition kinetics. More importantly, sacrificial interfacial S—S bonds undergo electrochemical reduction during cycling, generating an integrated SEI/PUMA interface that strengthens interfacial adhesion and maintains protection during both Zn deposition and resting. Consequently, PUMA@Zn symmetric cells cycle stably for 5080 h, while PUMA@Zn//Cu cells operate for over 4000 cycles with an average CE of 99.64%. The anionic sites also suppress polyiodide migration, enabling PUMA@Zn//I_2 cells to retain 88% capacity after 43 000 cycles and operate for over 11 000 cycles at an iodine loading of 16.58 mg cm^{-2}. These results demonstrate an effective strategy for constructing durable and reconfigurable hydrogel interfaces by integrating mechanical reinforcement, ion-transport regulation, and interfacial transformation within a single polymer network.

Author Contributions

Peng Li: conceptualization, methodology, software, data curation, investigation, validation, writing – original draft, formal analysis, visualization. **Jinping Wu**: investigation, methodology. **Zihan Zhu**: investigation, validation. **Jing Tang**: investigation, validation. **Ling Zhu**: investigation, formal analysis. **Liya Wang**: validation, investigation. **Xuan Tang**: validation, investigation. **Fangfang Ruan**: investigation, validation. **Huibing He**: investigation, resources. **Ning Zhao**: conceptualization, supervision, writing – review and editing. **Dongdong Li**: writing – review and editing, conceptualization, supervision, project administration, funding acquisition.

Acknowledgments

The authors thank the financial support from the National Science Fund for Distinguished Young Scholars (No.52325303) and the Natural Science Foundation of Guangxi Province (2026GXNSFBA00640125).

Conflicts of Interest

The authors declare no conflicts of interest.

Data Availability Statement

The data that support the findings of this study are available from the corresponding author upon reasonable request.

References

1. T. Jiang, D. Shen, Z. Zhang, et al., "Battery Technologies for Grid-Scale Energy Storage," *Nature Reviews Clean Technology* 1, no. 7 (2025): 474–492, https://doi.org/10.1038/s44359-025-00067-9.

2. Z. Zhu, T. Jiang, M. Ali, et al., "Rechargeable Batteries for Grid Scale Energy Storage," *Chemical Reviews* 122, no. 22 (2022): 16610–16751, https://doi.org/10.1021/acs.chemrev.2c00289.

3. H. Wu, J. Hao, S. Zhang, et al., "Aqueous Zinc–Iodine Pouch Cells With Long Cycling Life and Low Self-Discharge," *Journal of the American Chemical Society* 146, no. 24 (2024): 16601–16608, https://doi.org/10.1021/jacs.4c03518.

4. Y. Geng, Y. Han, H. Peng, et al., "Organic-Solvent-Free Weakly Solvating Electrolytes Enable Durable Ah-Scale Zn–Iodine Batteries Under Diverse Harsh Operating Conditions," *Journal of the American Chemical Society* 148, no. 22 (2026): 23118–23132, https://doi.org/10.1021/jacs.6c04647.

15213773, 0, Downloaded from https://onlinelibrary.wiley.com/doi/10.1002/anie.7908002 by Li Dongdong - Guangxi University , Wiley Online Library on [24/10/2026]. See the Terms and Conditions (https://onlinelibrary.wiley.com/terms-and-conditions) on Wiley Online Library for rules of use; OA articles are governed by the applicable Creative Commons License

5. D. Lin and Y. Li, "Recent Advances of Aqueous Rechargeable Zinc-Iodine Batteries: Challenges, Solutions, and Prospects," *Advanced Materials* 34, no. 23 (2022): 2108856, https://doi.org/10.1002/adma.202108856.

6. H. Chen, X. Li, K. Fang, H. Wang, J. Ning, and Y. Hu, "Aqueous Zinc-Iodine Batteries: From Electrochemistry to Energy Storage Mechanism," *Advanced Energy Materials* 13, no. 41 (2023): 2302187, https://doi.org/10.1002/aenm.202302187.

7. X. Yu, M. Chen, Z. Li, et al., "Unlocking Dynamic Solvation Chemistry and Hydrogen Evolution Mechanism in Aqueous Zinc Batteries," *Journal of the American Chemical Society* 146, no. 25 (2024): 17103–17113, https://doi.org/10.1021/jacs.4c02558.

8. X. Lu, G. Wang, B. Xu, et al., "Surface Engineering of Zinc Anodes Toward Durable Aqueous Zinc-Ion Batteries," *Advanced Functional Materials* 36, no. 49 (2026): e75763, https://doi.org/10.1002/adfm.75763.

9. H. Dai, T. Sun, J. Zhou, et al., "Unraveling Chemical Origins of Dendrite Formation in Zinc-Ion Batteries via In Situ/Operando X-Ray Spectroscopy and Imaging," *Nature Communications* 15, no. 1 (2024): 8577, https://doi.org/10.1038/s41467-024-52651-5.

10. S. Yao, Y. Zhang, H. Lu, et al., "Decoding the Electrodeposition of Zinc Anode With Dynamic Mixed Nucleation Model for Rechargeable Batteries," *Advanced Materials* 38, no. 21 (2026): e72783, https://doi.org/10.1002/adma.72783.

11. Y. Zhu, H. Zhang, M. Tao, et al., "A Universal Janus Biopolymer Separator Enabled Dual-Interfacial Regulation Toward Dendrite-Free and Shuttle-Free Zinc-Iodine Batteries," *Advanced Materials* 38, no. 24 (2026): e72959, https://doi.org/10.1002/adma.72959.

12. J. Kang, J. Zhang, W. Wan, et al., "A Dynamic Cathode Interlayer for Ultralow Self-Discharge and High Iodide Utilization in Zinc–Iodine Batteries," *Energy & Environmental Science* 18, no. 10 (2025): 4800–4810, https://doi.org/10.1039/d4ee05584e.

13. H. Zhao, D. Yin, Y. Qin, et al., "Highly Electrically Conductive Polyiodide Ionic Liquid Cathode for High-Capacity Dual-Plating Zinc–Iodine Batteries," *Journal of the American Chemical Society* 146, no. 10 (2024): 6744–6752, https://doi.org/10.1021/jacs.3c12695.

14. G. Chen, Y. Kang, H. Yang, et al., "Toward Forty Thousand-Cycle Aqueous Zinc-Iodine Battery: Simultaneously Inhibiting Polyiodides Shuttle and Stabilizing Zinc Anode Through a Suspension Electrolyte," *Advanced Functional Materials* 33, no. 28 (2023): 2300656, https://doi.org/10.1002/adfm.202300656.

15. L.-H. Pei, D.-M. Xu, Y.-Z. Luo, et al., "Zinc Single-Atom Catalysts Encapsulated in Hierarchical Porous Bio-Carbon Synergistically Enhances Fast Iodine Conversion and Efficient Polyiodide Confinement for Zn-I_2 Batteries," *Advanced Materials* 37, no. 10 (2025): 2420005, https://doi.org/10.1002/adma.202420005.

16. F. Wang, R. Ma, Z. Chen, et al., "Click Chemistry-Inspired Fixation Catalysis for Long-Life Zinc–Iodine Batteries," *Advanced Materials* 38, no. 2 (2026): e11980, https://doi.org/10.1002/adma.202511980.

17. Y. Liu, L. Zhang, L. Liu, et al., "All-Climate Energy-Dense Cascade Aqueous Zn–I_2 Batteries Enabled by a Polycationic Hydrogel Electrolyte," *Advanced Materials* 37, no. 46 (2025): 2415979, https://doi.org/10.1002/adma.202415979.

18. Y. Wang, Y. Cui, M. Zhao, et al., "Zwitterion-Mediated Interface Chemistry for Practical Zn-Iodine Batteries," *Nature Communications* 16, no. 1 (2025): 5565, https://doi.org/10.1038/s41467-025-60488-9.

19. S. Li, C. Sun, M. Zhang, et al., "An Integrated Tandem-Structured Separator Enables Dual-Enhanced Stable Interfaces for Long-Cycle-Life and High-Areal-Capacity Aqueous Zinc–Iodine Batteries," *Angewandte Chemie International Edition* 64, no. 33 (2025): e202506849, https://doi.org/10.1002/anie.202506849.

20. J.-L. Yang, H.-H. Liu, Y. Liu, et al., "A Bio-Chemical Synergy Strategy: Mycelium Separator Breaks the Coupled Degradation Cycle in Aqueous Zn–I_2 Batteries," *Advanced Materials* 38, no. 25 (2026): e72967, https://doi.org/10.1002/adma.72967.

21. Y. Qin, H. Li, C. Han, F. Mo, and X. Wang, "Chemical Welding of the Electrode–Electrolyte Interface by Zn-Metal-Initiated In Situ Gelation for Ultralong-Life Zn-Ion Batteries," *Advanced Materials* 34, no. 44 (2022): 2207118, https://doi.org/10.1002/adma.202207118.

22. H. Chen, L. Zhou, Y. Sun, et al., "Bio-Inspired Biomass Hydrogel Interface With Ion-Selective Responsive Sieving Mechanism for Corrosion-Resistant and Dendrite-Free Zinc-Iodine Batteries," *Energy Storage Materials* 76 (2025): 104113, https://doi.org/10.1016/j.ensm.2025.104113.

23. P. Chen, S. Jin, S. Hong, et al., "Adaptive Ion Channels Formed in Ultrathin and Semicrystalline Polymer Interphases for Stable Aqueous Batteries," *Journal of the American Chemical Society* 146, no. 5 (2024): 3136–3146, https://doi.org/10.1021/jacs.3c10638.

24. T. Mu, H. Lu, H. Wang, et al., "Artificial Organic-Inorganic Hybrid Interface Enables Reversible Zn Anodes," *Nano Energy* 138 (2025): 110835, https://doi.org/10.1016/j.nanoen.2025.110835.

25. S. Zhao, J. Wu, P. Lin, et al., "Applications of Polymers in Zinc Anode Protection for Aqueous Zinc-Ion Batteries," *Battery Energy* 5, no. 3 (2026): e70120, https://doi.org/10.1002/bte2.70120.

26. D.-Q. Cai, H. Wu, J.-L. Yang, T. Zhang, T. Xue, and H. J. Fan, "Dynamic Adaptive Interfaces Enable Zn-Iodine Hydrogel Batteries With High Areal Capacity and Low Self-Discharge," *Journal of the American Chemical Society* 148, no. 26 (2026): 27858–27868, https://doi.org/10.1021/jacs.6c09194.

27. C. Yan, L. Chen, W. Tian, D. Li, X. Wang, and N. Zhao, "Applications of Dynamic Polymers in Next-Generation High-Performance Lithium-Based Batteries," *Advanced Materials* 38, no. 54 (2026): e74011, https://doi.org/10.1002/adma.74011.

28. X. Yan, J. Zhang, Y. Sheng, et al., "Decoupling the Trade-Off Between Mechanical Properties and Ionic Conductivity in Hydrogel Polymer Electrolytes by Anomalous Water-Induced Microphase Separation," *ACS Nano* 19, no. 47 (2025): 40579–40593, https://doi.org/10.1021/acsnano.5c16323.

29. Y. Ai, C. Yang, Z. Yin, et al., "Biomimetic Superstructured Interphase for Aqueous Zinc-Ion Batteries," *Journal of the American Chemical Society* 146 (2024): 15496–15505, https://doi.org/10.1021/jacs.4c03943.

30. T. Shen, Z.-J. Chen, Y. Yang, et al., "Thinner-Than-Paper and Broad-Temperature-Adaptive Zinc-Iodine Batteries Enabled by Nanophase Separated Deep-Eutectic Hydrogel Electrolytes," *Nature Communications* 17, no. 1 (2026): 4827, https://doi.org/10.1038/s41467-026-71312-3.

31. X. Liu, Y. Ma, S. Chen, X. Liu, and Q. Zhang, "Closed-loop Recyclable and Robust Supramolecular Hydrogel Electrolytes With High Zinc Ion Mobility for Stable Zinc Anode," *Angewandte Chemie International Edition* 65, no. 37 (2026): e9230301, https://doi.org/10.1002/anie.9230301.

32. B. Sun, Y. Zong, K. Bao, et al., "Activating Gel Polymer Electrolyte Based Zinc-Ion Conduction With Filler-Integration for Advanced Zinc Batteries," *ACS Applied Materials & Interfaces* 15, no. 31 (2023): 37916–37924, https://doi.org/10.1021/acsami.3c06702.

33. S. Wu, M. Hua, Y. Alsaid, et al., "Poly(vinyl alcohol) Hydrogels With Broad-Range Tunable Mechanical Properties via the Hofmeister Effect," *Advanced Materials* 33, no. 11 (2021): 2007829, https://doi.org/10.1002/adma.202007829.

34. Y. Jin, S. Lu, X. Chen, et al., "Time-Salt Type Superposition and Salt Processing of Poly(methacrylamide) Hydrogel Based on Hofmeister Series," *Macromolecules* 57, no. 6 (2024): 2746–2755, https://doi.org/10.1021/acs.macromol.3c02395.

35. J. Liu, R. Wang, T. Li, et al., "Synergistic Hydrophobic and Hofmeister Effects Drive Recyclable, Tough, and Antiswelling Hydrogels for Underwater Communication," *ACS Macro Letters* 15, no. 4 (2026): 660–668, https://doi.org/10.1021/acsmacrolett.6c00140.

36. H. Zou, X. Meng, X. Zhao, and J. Qiu, "Hofmeister Effect-Enhanced Hydration Chemistry of Hydrogel for High-Efficiency Solar-Driven Interfacial Desalination," *Advanced Materials* 35, no. 5 (2023): 2207262, https://doi.org/10.1002/adma.202207262.

15213773, 0, Downloaded from https://onlinelibrary.wiley.com/doi/10.1002/anie.7908002 by Li Dongdong - Guangxi University , Wiley Online Library on [24/10/2026]. See the Terms and Conditions (https://onlinelibrary.wiley.com/terms-and-conditions) on Wiley Online Library for rules of use; OA articles are governed by the applicable Creative Commons License

37. L. Zhu, J. Tang, P. Li, et al., "Molecular Engineering-Enabled Self-Adaptive Topological Adsorption Interface: Synergistic Hydrophobic Nanoconfinement and Electrostatic Shielding for Highly Stable Zn Anode," *Advanced Functional Materials* 36, no. 40 (2026): e74981, https://doi.org/10.1002/adfm.74981.

38. C. Yan, L. Zhu, P. Li, et al., "Multi-Level Zn^{2+}-Buffering Interphase Enabled by Hierarchical Nanostructure Engineering of Gel Polymers for Highly Reversible Zinc Metal Anode," *Advanced Materials* 38, no. 4 (2026): e15316, https://doi.org/10.1002/adma.202515316.

39. Y. Mu, Y. Zhou, Y. Chu, et al., "Robust Piezoelectric-Derived Bilayer Solid Electrolyte Interphase for Zn Anodes Operating From −60 to 60°C," *ACS Nano* 19, no. 14 (2025): 14161–14176, https://doi.org/10.1021/acsnano.5c00178.

40. L. Chen, T. Xiao, J.-L. Yang, et al., "In-Situ Spontaneous Electropolymerization Enables Robust Hydrogel Electrolyte Interfaces in Aqueous Batteries," *Angewandte Chemie International Edition* 63, no. 21 (2024): e202400230, https://doi.org/10.1002/anie.202400230.

41. Z. Yang, Q. Zhang, T. Wu, et al., "Thermally Healable Electrolyte-Electrode Interface for Sustainable Quasi-Solid Zinc-Ion Batteries," *Angewandte Chemie International Edition* 63, no. 9 (2024): e202317457, https://doi.org/10.1002/anie.202317457.

42. Z. Chang, W. Xu, H. Wang, et al., "Dynamically Adaptive Interfacial Chemistry via Molecular Programming for Sustainable Zn Batteries," *Journal of the American Chemical Society* 148, no. 7 (2026): 7614–7624, https://doi.org/10.1021/jacs.5c21500.

43. F. Guo, C. Jin, H. Mi, et al., "Polyhydroxy Hydrogel Electrolyte With in Situ Tuned Interface Chemistry for Ultra-Stable Biosensing-Compatible Zinc Batteries," *Nano-Micro Letters* 18, no. 1 (2026): 217, https://doi.org/10.1007/s40820-025-02061-z.

44. X. Wang, M. Yang, Z. Ren, et al., "Mussel-Inspired, Hydrophobic Association-Regulated Hydrogel Electrolytes With Super-Adhesive and Self-Healing Properties for Durable and Flexible Zinc-ion Batteries," *Energy Storage Materials* 70 (2024): 103523, https://doi.org/10.1016/j.ensm.2024.103523.

45. Y. Lin, J. Huang, S. Wang, et al., "Stretchable, Adhesive, Anti-Freezing Hydrogel Electrolytes With Dual-Functional Water Regulation Enabled by Amide Group–Salt–Water Interactions for all-Climate Zinc-Ion Batteries," *Advanced Materials* 37, no. 41 (2025): e09975, https://doi.org/10.1002/adma.202509975.

46. H. Liu, F. Zhen, X. Yin, et al., "Ultra-Tough Dynamic Supramolecular Ion-Conducting Elastomer Induced Uniform Li^+ Transport and Stabilizes Interphase Ensures Dendrite-Free Lithium Metal Anodes," *Angewandte Chemie International Edition* 64, no. 2 (2025): e202414599, https://doi.org/10.1002/anie.202414599.

47. Y. Wang, J. Zhu, A. Chen, et al., "Spider Silk-Inspired Binder Design for Flexible Lithium-Ion Battery With High Durability," *Advanced Materials* 35, no. 47 (2023): 2303165, https://doi.org/10.1002/adma.202303165.

48. F. Pei, L. Wu, Y. Zhang, et al., "Interfacial Self-Healing Polymer Electrolytes for Long-Cycle Solid-State Lithium-Sulfur Batteries," *Nature Communications* 15, no. 1 (2024): 351, https://doi.org/10.1038/s41467-023-43467-w.

49. X. Xiang, L. Zhang, D. Sheng, et al., "Healable and Recyclable Polyurea-Urethane Elastomer With High Mechanical Robustness, Superhigh Elastic Restorability, and Exceptional Crack Tolerance," *Advanced Functional Materials* 34, no. 22 (2024): 2312571, https://doi.org/10.1002/adfm.202312571.

50. B. Li, B. Zhang, X. Bai, et al., "A Dynamic Self-Healing Protective Layer Enabling Stable Zinc Ion Batteries Through Strong Zn-S Affinity and Intramolecular Hydrogen Bonding," *Angewandte Chemie International Edition* 64, no. 29 (2025): e202503345, https://doi.org/10.1002/anie.202503345.

51. J.-L. Yang, T. Xiao, T. Xiao, et al., "Cation-Conduction Dominated Hydrogels for Durable Zinc–Iodine Batteries," *Advanced Materials* 36, no. 21 (2024): 2313610, https://doi.org/10.1002/adma.202313610.

52. Y. Wang, W. Yan, X. Zhu, et al., "Boosting Performance of Quasi-Solid-State Zinc Ion Batteries via Zincophilic Solubilization," *Angewandte Chemie International Edition* 64, no. 35 (2025): e202508556, https://doi.org/10.1002/anie.202508556.

53. C. Huyan, D. Liu, X. Han, et al., "Delayed Crystallization Response-Inspired Waterborne Polyurethane With High Performance," *Nature Communications* 16, no. 1 (2025): 9546, https://doi.org/10.1038/s41467-025-64573-x.

54. Y. Yan, S. Duan, B. Liu, et al., "Tough Hydrogel Electrolytes for Anti-Freezing Zinc-Ion Batteries," *Advanced Materials* 35, no. 18 (2023): 2211673, https://doi.org/10.1002/adma.202211673.

55. S. Zhang, D. Ren, Q. Zhao, et al., "Observation of Topological Hydrogen-Bonding Domains in Physical Hydrogel for Excellent Self-Healing and Elasticity," *Nature Communications* 16, no. 1 (2025): 2371, https://doi.org/10.1038/s41467-025-57692-y.

56. S. Guo, S. Zhu, Y. Qiao, et al., "Ultra-Low Hysteresis under Large Deformation Enabled by Fast Chains Relaxation in Highly Competitive Dynamic Hydrogen Bond Networks," *Advanced Science* 12, no. 36 (2025): e05417, https://doi.org/10.1002/advs.202505417.

57. J. Xie, Y. Ding, C.-C. Yan, et al., "Stiff, Tough, and Recyclable Self-Reinforced Polyurethane Plastics Based on Multiple Hydrogen Bonds Self-Assembly," *Advanced Functional Materials* 36, no. 49 (2026): e75851, https://doi.org/10.1002/adfm.75851.

58. K. Zhu, J. Luo, D. Zhang, et al., "Molecular Engineering Enables Hydrogel Electrolyte With Ionic Hopping Migration and Self-Healability Toward Dendrite-Free Zinc-Metal Anodes," *Advanced Materials* 36, no. 19 (2024): 2311082, https://doi.org/10.1002/adma.202311082.

59. K. Zhu, W. Zhuang, N. Wang, et al., "Rational Design of a Bilayer Interface for Long-Term Stability of Zn Anodes and MnO_2 Cathodes," *Advanced Materials* 37, no. 24 (2025): 2502366, https://doi.org/10.1002/adma.202502366.

60. S. Han, M. Li, Q. Fan, et al., "Multifunctional Additives With Dynamic Sacrificial S–S Bonds for Building Self-Assembled Monolayers of Zn-ion Batteries With Improved Stability and Longevity," *Energy & Environmental Science* 18, no. 9 (2025): 4186–4199, https://doi.org/10.1039/d4ee05922k.

61. T. Wang, P. Wang, L. Pan, et al., "Stabling Zinc Metal Anode With Polydopamine Regulation Through Dual Effects of Fast Desolvation and Ion Confinement," *Advanced Energy Materials* 13, no. 5 (2023): 2203523, https://doi.org/10.1002/aenm.202203523.

62. Z. Dai, X. Zhang, C. Yang, et al., "Enhancing Zinc Anode Stability via Self-Assembled Organic/Inorganic Hybrid Electrolyte Interfaces," *Advanced Energy Materials* 15, no. 38 (2025): e03193, https://doi.org/10.1002/aenm.202503193.

63. Z. Peng, S. Li, L. Tang, J. Zheng, L. Tan, and Y. Chen, "Water-Shielding Electric Double Layer and Stable Interphase Engineering for Durable Aqueous Zinc-ion Batteries," *Nature Communications* 16, no. 1 (2025): 4490, https://doi.org/10.1038/s41467-025-59830-y.

64. J. Chen, Y. Shi, S. Zheng, et al., "Blocking Interfacial Proton Transport via Self-Assembled Monolayer for Hydrogen Evolution-Free Zinc Batteries," *Angewandte Chemie International Edition* 63, no. 26 (2024): e202404825, https://doi.org/10.1002/anie.202404825.

65. J. Lee, M. Lee, B. Kim, et al., "Tailored Polymer-Based SEI via iCVD for Stable Zinc Metal Anodes in Aqueous Batteries Through Modulation of Hydrophilicity and Elasticity to Inhibit Hydrogen Evolution Reactions," *Advanced Functional Materials* 36, no. 2 (2026): e07730, https://doi.org/10.1002/adfm.202507730.

66. X. Cai, X. Li, J. Liang, et al., "Stabilizing the Anode and Cathode Interface Synchronously via Electrolyte-Triggered Hydrogel Interphase for Zinc Metal Batteries," *Nano-Micro Letters* 18, no. 1 (2026): 206, https://doi.org/10.1007/s40820-025-02051-1.

67. D. Xie, Z.-W. Wang, Z.-Y. Gu, et al., "Polymeric Molecular Design towards Horizontal Zn Electrodeposits at Constrained 2D Zn^{2+} Diffusion: Dendrite-Free Zn Anode for Long-Life and High-Rate Aqueous Zinc

15213773, 0, Downloaded from https://onlinelibrary.wiley.com/doi/10.1002/anie.7908002 by Li Dongdong - Guangxi University , Wiley Online Library on [24/10/2026]. See the Terms and Conditions (https://onlinelibrary.wiley.com/terms-and-conditions) on Wiley Online Library for rules of use; OA articles are governed by the applicable Creative Commons License

Metal Battery," *Advanced Functional Materials* 32, no. 32 (2022): 2204066, https://doi.org/10.1002/adfm.202204066.

68. W. Fan, C. Zhu, X. Wang, et al., "All-natural Charge Gradient Interface for Sustainable Seawater Zinc Batteries," *Nature Communications* 16, no. 1 (2025): 56519, https://doi.org/10.1038/s41467-025-56519-0.

69. Y. Li, H. Xu, X. Li, et al., "Molecular Damping Effect of Trace Additives Enhances Zinc Anode Stability under High Depth of Discharge," *Advanced Science* 12, no. 37 (2025): 202507071, https://doi.org/10.1002/advs.202507071.

70. M. Xu, X. He, S. Xue, et al., "Unveiling Ion Pairing Reorganization Mechanism of Oxygen Vacancy-Rich Amorphous Molybdenum Oxide-Based Solid-Electrolyte Interphase for Fast Zn^{2+} Desolvation," *Advanced Energy Materials* 16, no. 2 (2026): e03167, https://doi.org/10.1002/aenm.202503167.

71. R. Pan, Y. Xie, B. Jiang, et al., "Flexible and Dynamic Interfacial Desolvation in High-Entropy Electrolyte for Dendrite-Free Aqueous Zinc-Ion Batteries," *Advanced Materials* 38, no. 2 (2026): e12633, https://doi.org/10.1002/adma.202512633.

72. C. Li, Y. Liu, J. Liu, et al., "Well-Aligned Liquid Crystal Interface and Expanded Solvation Sheath Accelerate Zn^{2+} Desolvation Kinetics for Stable Zinc Batteries," *Journal of the American Chemical Society* 147, no. 31 (2025): 27640–27650, https://doi.org/10.1021/jacs.5c06049.

73. R. Liu, C. Wang, F. Wan, et al., "Hydrogen-Bond-Rich Supramolecular Multiblock Copolymers Facilitate Rapid Zn^{2+} Migration in Quasi-Solid-State Zinc-Ion Batteries," *Advanced Functional Materials* 36, no. 16 (2026): e17166, https://doi.org/10.1002/adfm.202517166.

74. Q. Nian, X. Luo, D. Ruan, et al., "Highly Reversible Zinc Metal Anode Enabled by Strong Brønsted Acid and Hydrophobic Interfacial Chemistry," *Nature Communications* 15, no. 1 (2024): 4303, https://doi.org/10.1038/s41467-024-48444-5.

75. J. L. Yang, J. Li, J. W. Zhao, K. Liu, P. Yang, and H. J. Fan, "Stable Zinc Anodes Enabled by a Zincophilic Polyanionic Hydrogel Layer," *Advanced Materials* 34, no. 27 (2022): 2202382, https://doi.org/10.1002/adma.202202382.

76. M. Kim, J. Lee, Y. Kim, Y. Park, H. Kim, and J. W. Choi, "Surface Overpotential as a Key Metric for the Discharge–Charge Reversibility of Aqueous Zinc-Ion Batteries," *Journal of the American Chemical Society* 145, no. 29 (2023): 15776–15787, https://doi.org/10.1021/jacs.3c01614.

77. Y. Wang, K. Zhong, J. Zhang, et al., "Concomitant Zinc Dendrite Mitigation and Iodide Shuttle Confinement: A Bifunctional Zwitterionic Hydrogel Electrolyte Unlocking Ultralong-Cycling Aqueous Zinc-Iodine Batteries," *Advanced Functional Materials* 36, no. 26 (2026): e26937, https://doi.org/10.1002/adfm.202526937.

78. C. Tian, J. Wang, R. Sun, et al., "Improved Interfacial Ion Migration and Deposition Through the Chain-Liquid Synergistic Effect by a Carboxylated Hydrogel Electrolyte for Stable Zinc Metal Anodes," *Angewandte Chemie International Edition* 62, no. 42 (2023): e202310970, https://doi.org/10.1002/anie.202310970.

79. M. Yang, Y. Zhang, Q. Li, X. Wang, B. Ma, and Z. Niu, "The Design of Interfacial Organic-Riched Phase by Molecular Interlocking for Stable Zn Anodes," *Angewandte Chemie International Edition* 64, no. 37 (2025): e202512032, https://doi.org/10.1002/anie.202512032.

80. Y. Gao, N. Yang, F. Bu, et al., "Double-Sided Engineering for Space-Confined Reversible Zn Anodes," *Energy & Environmental Science* 17, no. 5 (2024): 1894–1903, https://doi.org/10.1039/d3ee04292h.

81. S. D. Pu, B. Hu, Z. Li, et al., "Decoupling, Quantifying, and Restoring Aging-Induced Zn-Anode Losses in Rechargeable Aqueous Zinc Batteries," *Joule* 7, no. 2 (2023): 366–379, https://doi.org/10.1016/j.joule.2023.01.010.

82. Y.-F. Qu, J.-W. Qian, F. Zhang, et al., "Constructing 3D Crosslinked Macromolecular Networks as a Highly Efficient Interface Layer for Ultra-Stable Zn Metal Anodes," *Advanced Materials* 37, no. 1 (2025): 2413370, https://doi.org/10.1002/adma.202413370.

83. B. Chen, X. Cheng, H. Yang, et al., "Reviews of High-Longevity Aqueous Zinc Metal Batteries Achieved by Programmable Interface Architectures," *Energy & Environmental Materials* 9, no. 2 (2026): e70176, https://doi.org/10.1002/eem2.70176.

84. C. Ma, C. Dong, P. Zhao, et al., "Zincophilic Nanowire Array with Hydrophobic Iodine Elimination Layer for Ultrastable Zinc-Iodine Battery," *Advanced Materials* 38, no. 23 (2026): e20465, https://doi.org/10.1002/adma.202520465.

85. Y. Liao, H.-C. Chen, C. Yang, et al., "Unveiling Performance Evolution Mechanisms of MnO_2 Polymorphs for Durable Aqueous Zinc-ion Batteries," *Energy Storage Materials* 44 (2022): 508–516, https://doi.org/10.1016/j.ensm.2021.10.039.

86. A. Zhang, R. Zhao, Y. Wang, et al., "Hybrid Superlattice-Triggered Selective Proton Grotthuss Intercalation in δ-MnO_2 for High-Performance Zinc-Ion Battery," *Angewandte Chemie International Edition* 62, no. 51 (2023): e202313163, https://doi.org/10.1002/anie.202313163.

Supporting Information

Additional supporting information can be found online in the Supporting Information section.

Additional experimental details, computational methods, material characterization, electrochemical measurements, supplementary figures, and performance-comparison tables (PDF).

Supporting File: anie75437-sup-0001-SuppMat.pdf.

15213773, 0, Downloaded from https://onlinelibrary.wiley.com/doi/10.1002/anie.7908002 by Li Dongdong - Guangxi University , Wiley Online Library on [24/10/2026]. See the Terms and Conditions (https://onlinelibrary.wiley.com/terms-and-conditions) on Wiley Online Library for rules of use; OA articles are governed by the applicable Creative Commons License